Koo et al. *Light: Science & Applications* (2024)13:30
https://doi.org/10.1038/s41377-024-01380-x

Official journal of the CIOMP 2047-7538
www.nature.com/lsa

REVIEW ARTICLE Open Access

Dynamical control of nanoscale light-matter interactions in low-dimensional quantum materials

Yeonjeong Koo[1], Taeyoung Moon[1], Mingu Kang[1], Huitae Joo[1], Changjoo Lee[1], Hyeongwoo Lee[1], Vasily Kravtsov[2] and Kyoung-Duck Park[1]✉

Abstract

Tip-enhanced nano-spectroscopy and -imaging have significantly advanced our understanding of low-dimensional quantum materials and their interactions with light, providing a rich insight into the underlying physics at their natural length scale. Recently, various functionalities of the plasmonic tip expand the capabilities of the nanoscopy, enabling dynamic manipulation of light-matter interactions at the nanoscale. In this review, we focus on a new paradigm of the nanoscopy, shifting from the conventional role of imaging and spectroscopy to the dynamical control approach of the tip-induced light-matter interactions. We present three different approaches of tip-induced control of light-matter interactions, such as cavity-gap control, pressure control, and near-field polarization control. Specifically, we discuss the nanoscale modifications of radiative emissions for various emitters from weak to strong coupling regime, achieved by the precise engineering of the cavity-gap. Furthermore, we introduce recent works on light-matter interactions controlled by tip-pressure and near-field polarization, especially tunability of the bandgap, crystal structure, photoluminescence quantum yield, exciton density, and energy transfer in a wide range of quantum materials. We envision that this comprehensive review not only contributes to a deeper understanding of the physics of nanoscale light-matter interactions but also offers a valuable resource to nanophotonics, plasmonics, and materials science for future technological advancements.

Introduction

Low-dimensional quantum materials, such as two-dimensional (2D) transition metal dichalcogenides (TMDs), semiconductor nanowires, and quantum dots (QDs) have garnered significant attention due to their exceptional optical, electrical, and structural properties[1–4]. Their unique properties are inherited from the reduced dimensionality, which leads to the new physical phenomena, such as the increased quantum confinement effect[5] and decreased dielectric screening effects[6]. These characteristics exhibit remarkable sensitivity to external engineering strategies, offering wide tunability that distinguishes them from their bulk counterparts[7,8]. By leveraging the tunability, we can precisely control their optical response[9,10], electrical conductivity[11,12], and structural characteristics[13,14], rendering them promising candidates for a multitude of applications in nanophotonics, optoelectronics, and beyond.

Since the length scale of the interesting phenomena reduces down to the nanoscale, the intriguing physical processes of low-dimensional quantum materials cannot be investigated by the conventional microscale spatial imaging methods. Nanoscopy approaches, such as scanning probe microscopy (SPM)[15–19] and tip-enhanced spectroscopy[20–24], have enabled us to directly visualize the nanoscale characteristics of the low-dimensional quantum materials with extraordinary accessibility. Using the plasmonic tip, nanoscopy allows for the spatially resolved characterizations of the electronic structure, excitonic properties, and local optical responses of the materials. This capability has revealed a wealth of interesting physical phenomena at the nanoscale, including exciton dynamics,

Correspondence: Kyoung-Duck Park (parklab@postech.ac.kr)
[1]Department of Physics, Pohang University of Science and Technology (POSTECH), Pohang 37673, Republic of Korea
[2]School of Physics and Engineering, ITMO University, Saint Petersburg 197101, Russia
These authors contributed equally: Yeonjeong Koo, Taeyoung Moon

quantum confinement effects, and the interplay between electronic and optical properties. For instance, the ability to probe the optically dark states, which are typically challenging to access, opens up possibilities for the manipulation of light emission and tailored photon sources[25–27]. Nanoscopy also unveils the drift-dominant exciton funneling facilitated by the nanoscale strain, providing insights into strain engineering for improved optoelectronic devices[28–30]. Moreover, achieving strong coupling with nanoscale mode volumes allows for the exploration of cavity quantum electrodynamics effects, enabling precise control over light-matter interactions at the fundamental level[31–33].

However, a plethora of physics captured by the conventional nanoscopy is just the tip of the iceberg, whereas the complex interplay between multiple degrees of freedom, such as electronic, vibrational, and photonic modes, as well as their coupling dynamics remain largely unexplored. Therefore, there is a growing demand for innovative approaches to actively manipulate the light-matter interactions. In this review, we discuss the recent progress on the dynamic control of tip-induced light-matter interactions, especially for the low-dimensional quantum materials. As illustrated in Fig. 1b, we divide the main text into three parts based on the type of tip-induced control, i.e., gap control of tip-cavity, tip-pressure control, and near-field polarization control. For low-dimensional semiconductors, such as 0D QDs and 2D TMDs, we discuss the modulation of radiative emission depending on the variation of tip-sample distance (part 1) and the modified strain and band gap properties induced by the GPa scale tip-pressure (part 2). Additionally, we discuss the near-field polarization control at the tip apex achieved by the geometrical tip modification and adaptive wavefront shaping of the excitation beam (part 3). We believe that this review will guide the future direction of manipulation of the quantum light-matter interaction by introducing a new paradigm of near-field microscopy and suggesting the recently developed approaches to discover the hidden nature of the emerging quantum materials.

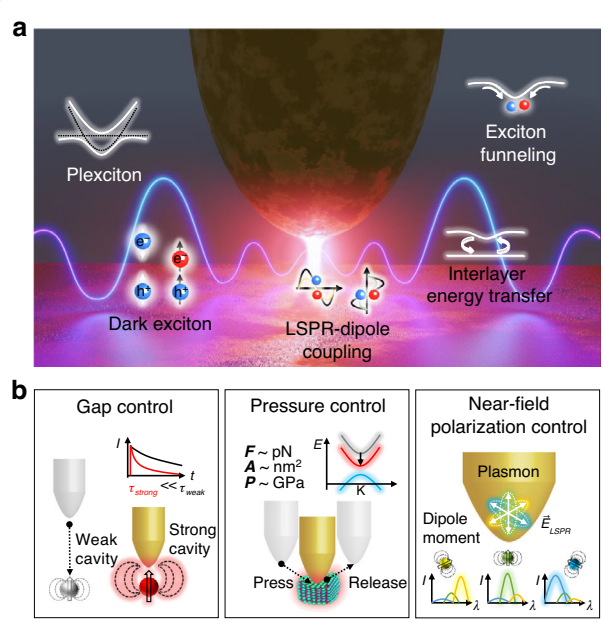

Fig. 1 Illustration of dynamic tip-induced control of light-matter interactions. a Unique properties of low-dimensional quantum materials that can be dynamically manipulated by the tip-induced control. **b** Schematic illustrations for the three types of tip-induced control. Gap control for engineering the cavity-emitter coupling strength, pressure control for engineering the strain, bandgap, and emission energy of quantum materials, and near-field polarization control for engineering the plasmon-emitter coupling with high selectivity

Tip-induced control of radiative emissions via cavity-gap engineering

Many types of light-matter interaction play a crucial role in photonic and optoelectronic device applications, e.g., lasers, light-emitting diodes (LEDs), single photon emitters, photodiodes, and solar cells[34–38]. Since plasmonic cavities can modify light-matter interactions with the nanoscale mode volume, cavity-quantum electrodynamics (cavity-QED) study with many different platforms, such as nanoparticles on mirror (NPoM)[39–44], bowtie antennas[45–51], and nanogap structures[52–58], has become ever more important. However, the static geometry of the conventional plasmonic cavities highly restricts the dynamic controllability of light-matter interactions, e.g., Purcell enhancement[48,59–66], radiative decay rate[57,67–74], and coupling strength[33,42,43,47,49,75–80], due to their fixed cavity mode volume. Hence, to achieve the desired nanoscale modulation of the cavity-gap in a reversible manner, the plasmonic tip-cavity approach combined with a SPM has been demonstrated.

Figure 2a-(i) shows the schematic illustration of the tip-enhanced Raman scattering (TERS) and photoluminescence (TEPL) spectroscopy based on the shear-force atomic force microscopy (AFM) to investigate the tip-induced optical responses of a TMD monolayer[81]. When the Au tip closely approaches the emitters, the optical excitation rate (Γ_e) is enhanced due to the field localization effect, which promotes the interaction of the light with the phonon and exciton. The distance-dependent excitation rate is well-described with an equation $\Gamma_e(z) \propto (1/(R+z))^4$ with the tip apex radius R and tip-sample distance z. In this condition, TERS and TEPL signals are additionally enhanced by different mechanisms. In the case of TERS, the charge-transfer resonance between the TMD monolayer and the metal tip enhances the Raman scattering[82]. For TEPL, the spontaneous emission rate is increased by the Purcell effect with the well-known Purcell factor $F_p \propto Q/V$, where Q and V

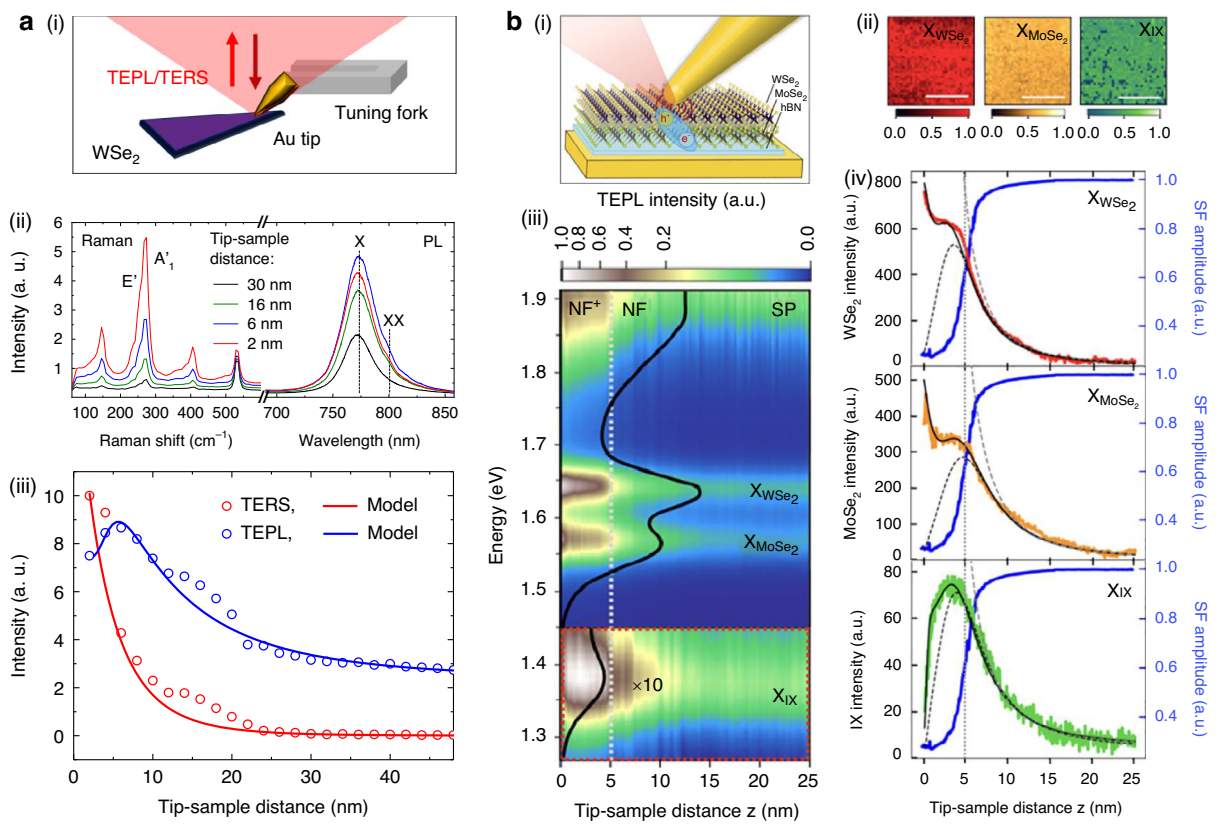

Fig. 2 Tip-induced control of photoluminescence and Raman scattering via cavity-gap engineering. a Manipulation of the TERS/TEPL response of a WSe_2 monolayer. (i) Schematic of the tip-enhanced nano-spectroscopy. (ii) TERS/TEPL spectra at the selected typical tip-sample distances. (iii) Evolution of the TERS/TEPL intensity of a WSe_2 monolayer as the tip-sample distance decreases, fitted with the rate equation model. **b** Purcell effect-induced TEPL manipulation of a TMD heterostructure. (i) Schematic of tip-enhanced nanocavity clock spectroscopy. (ii) TEPL images of the heterobilayer for the integrated intensity of X_{WSe_2} (red), X_{MoSe_2} (yellow), and X_{IX} (green). Scale bar is 500 nm. (iii) Evolution of TEPL spectra with respect to the tip-sample distance *z*. (iv) Distance-dependent PL intensity of X_{WSe_2}, X_{MoSe_2}, and X_{IX}, fitted with the coupled rate equation model. **a** Reproduced with permission[81]. Copyright [2016] American Chemical Society. **b** Reproduced with permission[86]. Copyright [2021] American Chemical Society

are the quality factor of an emitter and the mode volume of a cavity. Figure 2a-(ii) shows the distance-dependent TERS/TEPL spectra of a WSe_2 monolayer at the selected distances between the tip and sample. By modulating the tip-sample distance, the intensity of the TERS/TEPL can be adjusted to the desired level. Furthermore, the experimental data of the TERS/TEPL intensity with respect to the tip-sample distance shows a good agreement with the simulation data, as shown in Fig. 2a-(iii). The gradual enhancement of the TERS/TEPL intensity with the decreasing tip-sample distance at $d < 20$ nm can be explained by the rate equation for excited state population of the phonons and excitons coupled with the tip-plasmon. However, at the distance $d < 5$ nm, the PL intensity is decreased due to the near-field polarization transfer between the WSe_2 exciton and the metal tip causing nonradiative damping and PL quenching. PL quenching is a classical phenomenon that occurs due to near-field energy transfer from a semiconductor to a metal, leading to nonradiative decay. In addition, a transition from the classical regime to the quantum regime occurs at smaller gaps, primarily driven by nonlocal screening and charge tunneling effects, as elucidated in previous research[83]. Nonlocal screening pertains to the behavior of electrons in a metal and how they interact with screen charges at the metal-semiconductor gap. This phenomenon can cause deviations in the spatial distribution of electron gas within the metal structure compared to the geometric boundaries, resulting in a decrease of TEPL intensity at smaller gaps[84,85]. Quantum tunneling, on the other hand, is a well-known electron behavior in sub-nanometer gaps, contributing to nonradiative decay of excitons in the semiconductor via charge transfer to the metallic tip in TEPL experiments. The distance-dependent change in TEPL from the classical to the quantum regime can be effectively described by modified rate equation models, as evidenced in prior studies[81,84]. This study demonstrated the near-field light-

matter interactions in a TMD monolayer with TEPL and TERS, revealing the potential of tip-induced cavity-gap engineering for modulating nano-optical properties of emerging 2D materials.

The similar tip-induced approach was also employed to control the light-matter interactions in a TMD heterobilayer, especially by manipulating competing TEPL responses of intra- and inter-layer excitons. As shown in Fig. 2b, May et al.[86] investigated TEPL properties of the $WSe_2/MoSe_2$ heterostructure. First of all, the spatially homogeneous region over a 1 μm^2 was confirmed through the TEPL imaging (Fig. 2b-(ii)). Then, the authors were able to manipulate the TEPL spectra of intralayer excitons (X_{WSe_2} and X_{MoSe_2}), interlayer exciton (X_{IX}), and surface plasmon (SP) as a function of the tip-sample distance z from 25 nm to 0 nm, as shown in Fig. 2b-(iii). From the measurement results, the authors could classify the near-field responses of the heterobilayer into three ranges depending on z: (1) a range of near-field (NF) ($z \geq 5$ nm), (2) a range of suppressed enhancement (1 nm $< z <$ 5 nm), and (3) a NF^+ range ($z \leq 1$ nm). In the NF range, PL intensity of X_{WSe_2}, X_{MoSe_2}, and X_{IX} is continuously enhanced as the increasing excitation rate dominates over PL quenching in the proximity of the Au tip. In the range of 1 nm $< z <$ 5 nm, the PL quenching has a predominance of the near-field response over the increased excitation rate via dipole coupling of the Au tip and ultrafast ohmic Drude damping. By contrast, the strong Purcell effect enhances the spontaneous emission rate in the range of $z \leq 1$ nm (NF^+ region). Interestingly, in this region, only the TEPL of intralayer excitons is largely increased due to Purcell enhancement. Concurrently, the X_{IX} are quenched, because the tip-enhanced nonradiative damping of X_{IX} becomes much faster than the intralayer charge transfer. This complex competing spectral behaviors of X_{IX}, X_{WSe_2}, and X_{MoSe_2} with respect to the decreasing z is modeled by the coupled rate equations, as shown in Fig. 2b-(iv). This work presents a method for controlling the radiative emission of complex quantum systems solely by dynamically modulating the tip-sample distance. Moreover, the proposed method can be applied to investigate the dynamics of excitonic systems in a wide range of materials.

In addition to the bright excitons, the strong out-of-plane optical field at the tip-cavity can reveal the forbidden optical states in 2D TMDs. Park et al.[25] demonstrated the first work of tip-induced probing and controlling the room temperature dark exciton (X_D) radiation in a WSe_2 monolayer, which typically exhibits the spin-forbidden nonradiative decay with the intrinsic out-of-plane oriented transition dipole moment. Following that, the recent study of Hasz et al.[26] showed the tip-induced X_D radiation in nano-bubbles of a WSe_2 monolayer (Fig. 3a-(i)). The physical mechanism of the tip-induced radiative control of the X_D is divided into two steps as follows. First, the linearly polarized incident light is strongly confined in the tip-cavity formed with the metal substrate resulting in the large enhancement of the out-of-plane optical field due to the dipole-dipole interaction. The confined light then effectively excites the vertically oriented X_D in the WSe_2 monolayer. Additionally, the spontaneous emission rate of the X_D is increased by the Purcell effect, which, in general, gives maximum enhancement when the orientation of the emitter aligns with the polarization axis of the localized fields. Therefore, the Purcell effect of X_D in the tip-cavity achieved an extraordinarily large enhancement of the radiative emission rate. In addition, as illustrated in Fig. 3a-(i), a side-illumination TEPL geometry is particularly advantageous for the effective collection of dark exciton emissions, which possess a k-vector parallel to the 2D surface. Note that the lower bandgap energy of X_D compared to X_0 can be attributed to the spin-forbidden transition to the lower-energy conduction band. The degree of confinement of the incident light and the enhancement of the radiative emission rate sensitively depends on the cavity-gap, as described previously. Therefore, the radiative emission rate of X_D is controlled by modulating the tip-sample distance, as shown in Fig. 3a-(ii). Figure 3a-(iii) shows the two extracted TEPL spectra from Fig. 3a-(ii) at different distances of the tip and sample. For the 10 nm of tip-sample distance (green), only the bright exciton emission is observed. By contrast, as the tip-sample distance is decreased, X_D emission is observed, while the intensity of the bright exciton decreases due to dipole coupling and energy transfer with Drude relaxation in the metal substrate and tip. Therefore, the forbidden optical state in conventional light-matter coupling was allowed to be brightened via nanoscale engineering of the tip-cavity gap. Through the dynamical engineering of radiative emission of X_D at room temperature, we envision many different types of device applications in quantum nano-optoelectronics, utilizing its long radiative lifetime and coherence time. Since these studies were light-matter interaction phenomena in the weak coupling regime, one could only observe modifications in optical intensity induced by the coupling of plasmon with excitons and phonons. In the strong coupling regime, on the other hand, the modifications in photon energy can also be pronouncedly observed in addition to the tip-enhanced optical responses. However, because of its dominant out-of-plane optical field in the cavity-gap, tip-cavity is less advantageous for the strong coupling with in-plane excitons in 2D materials. While metasurfaces have been suggested for achieving strong coupling with in- plane excitons[87], tip-cavity has stood out as a suitable platform for the out-of-plane dipole emitter, such as QD. Park et al.[31] introduced a concept of tip-enhanced strong coupling (TESC) spectroscopy, by forming a nanoscale

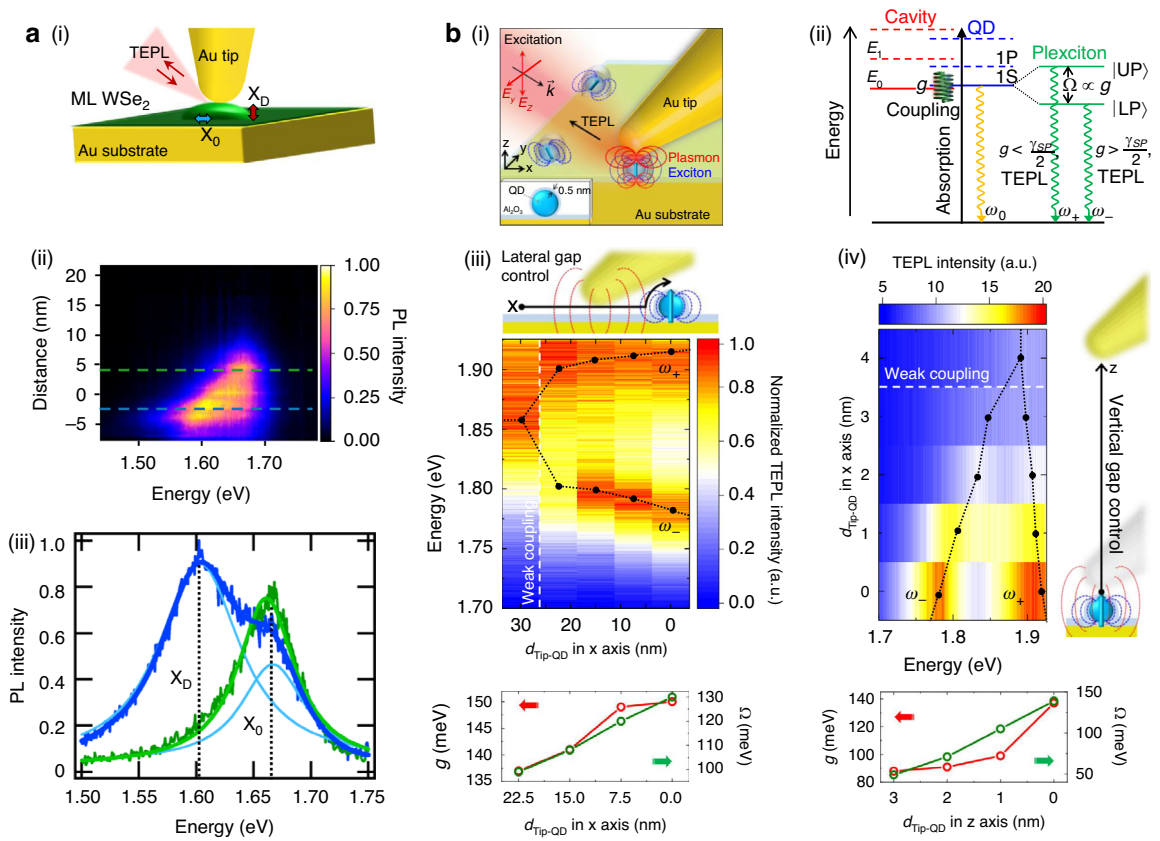

Fig. 3 Tip-induced control of radiative emission of dark exciton and strong coupling of quantum dot exciton via cavity-gap engineering. a Probing radiative emission of the dark exciton (X_D) in a WSe_2 monolayer via TEPL. (i) Schematic of the TEPL to probe and control X_D in a TMD nanobubble. (ii) Continuous plot of TEPL spectra with respect to the tip-sample distance. (iii) TEPL spectra at different tip-sample distances indicated by dotted lines in (**a**-(ii)). **b** Control of the strong coupling between the tip-cavity and the single quantum emitter. (i) Schematic of the TESC spectroscopy. (ii) Energy diagram of the tip-cavity, QD, and the polariton state of plasmon and exciton, i.e., plexciton. Modified TEPL spectra depending on the lateral (iii) and the vertical (iv) tip-sample distance change. **a** Reproduced with permission[26]. Copyright [2023] American Chemical Society. **b** Reprinted with permission[31]. Copyright © 2019 Park et al., some rights reserved; exclusive licensee American Association for the Advancement of Science. No claim to original U.S. Government Works. Distributed under a Creative Commons Attribution NonCommercial License 4.0 (CC BY-NC)

tip-cavity for a single emitter. In this study, a single CdSe/ZnS QD was placed between the Au tip and the Au surface, as illustrated in Fig. 3b-(i). Since this Au-Au junction provides a nanoscale mode volume in the tip-cavity, it can induce strong coupling between the cavity plasmon and the QD exciton. To induce the strong coupling state, the transition dipole moment of a QD should be also oriented vertically (along the tip-cavity axis) because the coupling strength (g) depends on the dipole orientation of the excitons ($\vec{\mu}$) and plasmon polarization ($\vec{E}_0$)[88]:

$$\hbar g \propto \vec{\mu} \cdot \vec{E}_0 \propto \vec{\mu} \cdot \vec{u}_{\mathrm{cav}} \sqrt{\frac{N\hbar\omega_{\mathrm{exc}}}{\epsilon_0 V}} \quad (1)$$

where $\vec{u}_{\mathrm{cav}}$ is the unit vector of the plasmon polarization of the cavity, N is the number of molecules, ϵ_0 is the vacuum permittivity, $\hbar\omega_{\mathrm{exc}}$ is the exciton energy, and V is the cavity mode volume. As shown in the energy diagram of Fig. 3b-(ii), when the coupling strength is larger than the loss of the coupled system, one can facilitate the plexciton state, i.e., strong coupling state of plasmon and exciton, which shows a signature of Rabi splitting in TEPL spectra. The beauty of TESC spectroscopy compared to strong coupling studies using static plasmonic cavities[33,42,43,47,49,75–80] is dynamic controllability of the strong coupling state. The authors could control the coupling strength of plexcitons by modulating the optical mode volume V through the cavity-gap engineering in a few nm scales ($g \propto 1/\sqrt{V}$) because the Au tip can move laterally or vertically by the AFM control. TEPL spectra in Fig. 3b-(iii), (iv) demonstrate the continuous modifications in coupling strength for the plexciton state, when the tip-cavity mode volume gradually changes. For the single isolated CdSe/ZnS QD in the TESC spectroscopy,

the coupling strength of ~140 meV was observed at room temperature. The coupling strength is derived by using the coupled harmonic oscillator model with Weisskopf-Wigner approximation[89]:

$$I_{PL}(\omega) = \frac{\gamma_{QD}}{2\pi}\left|\frac{\gamma_{SP}/2 - i(\omega - \omega_{SP})}{\left(\gamma_{SP} + \gamma_{QD}\right)/4 - i(\omega_{QD} - \omega_{SP})/2 - i(\omega - \omega_{QD})^2 + \Omega^2}\right|^2 \quad (2)$$

$$g = 2\sqrt{\Omega^2 - \frac{(\omega_{QD} - \omega_{SP})^2}{4} + \frac{\left(\gamma_{SP} - \gamma_{QD}\right)^2}{16}} \quad (3)$$

where Ω, ω_{SP}, γ_{QD}, and γ_{SP} denote the vacuum Rabi frequency, the resonance frequency of QD, the resonance frequency of cavity, the decay rate of QD, and the decay rate of cavity, respectively.

This work presented a modulation of coupling strength through plasmonic cavity-gap engineering allowing for the control of the Rabi splitting in a strong coupling regime. The other advantage of TESC compared to conventional static cavities is the ability to perform a control experiment. That is, one can induce tip-enhanced strong coupling for many different emitters with the 3D movable tip-cavity, which enables control experiments in the strong coupling regime. Hence, this approach enables the tuning of quantum-optical interfaces and provides a large degree of functionality to control quantum dynamics, which can lead to the advanced development of quantum computing. Furthermore, quantum plasmonic effects in sub-nm gaps should be briefly introduced. As the cavity-gap decreases down to the quantum tunneling regime, quantum plasmonic effects play a pivotal role in light-matter interactions, leading to unique and often non-classical phenomena under this extreme cavity condition[83]. For example, a transition from plasmonic enhancement to electron tunneling was observed in a tip-cavity. In an insightful study by Kravtsov et al.[84], the authors measured luminescence signals using a gold tip positioned above a flat gold surface while changing the tip-sample gap. Their observations revealed that the peak luminescence intensity was attained when the tip was at an approximate gap distance of $d \sim 1.5$ nm. Notably, as the gap width reduced, PL quenching became evident, and concurrently, the luminescence spectral peaks exhibited a blue-shift, signaling the onset of electron tunneling. In addition, Zhe et al. demonstrated exciton-to-trion conversion in a TMD monolayer by using the electron tunneling regime of tip-cavity[90]. Their experimental observations underscore the fundamental distinctions between classical and quantum plasmonic regimes in the study of light-matter interactions. Classical TEPL facilitates nano-spectroscopy through plasmonic near-field enhancement but provides limited capacity to locally manipulate the excitons in 2D semiconductors. In contrast, the quantum plasmonic TEPL technique offers novel control mechanisms alongside classical nano-spectroscopy capabilities, thereby unlocking fresh avenues for concurrent nano-imaging and control within the quantum domain. Therefore, considering the unique quantum plasmonic behaviors of the sub-nm gap tip-cavity will open up exciting possibilities for investigating phenomena that were previously inaccessible. Moreover, in the quantum regime, the tip-induced approach can be used to investigate the tunneling effect in biomolecules[91,92]. However, embedding biomolecules in the gap between the tip and substrate is not an easy process, particularly in achieving reproducibility and stability. Recently, hyperspectral TERS imaging of single molecules at room temperature has been made possible by improved reproducibility via a freeze-frame approach using a thin Al_2O_3 capping layer[93], yet dynamic control of light-biomolecule interactions remains challenge. Conversely, the use of static nanogap structures, coupled with the application of dynamic control factors like external electric and optical fields, offers distinct advantages, compared to tip-induced approach, when it comes to probing quantum effects within the tunneling region of biomolecules[94,95]. These recent studies are compelling examples demonstrating how this approach provides a new avenue for investigating the intricate interplay between biological molecules and light-matter interactions, ultimately leading to a deeper comprehension of these complex phenomena.

In summary, the recently demonstrated works on tip-induced control of radiative emissions via cavity-gap engineering provide a new direction for the cavity-QED studies. In contrast to the static plasmonic cavity, the dynamically modulating mode volume in the tip-cavity enables a systematic manipulation of the plasmon-coupled optical properties for various emitters, such as spontaneous emission rate, energy transfer, coupling strength, and so forth. Specifically, strong coupling significantly modifies the chemical reaction rate of molecules[96], emission rate of single quantum dot[97], and emission properties of 2D TMDs[42]. Therefore, we envision that the tunability of tip-cavity for a range of light-matter interactions at the nanoscale provides a new strategy for the next-generation nano-photonic device applications, overcoming the current performance limits of optoelectronic devices.

Tip-induced control of excitons via GPa-scale pressure engineering

Strain engineering has emerged as a versatile method to modify the physical properties of materials, expanding their potential applications in various nano-optoelectronic devices[98–100]. Although several

techniques, such as thermal annealing[101,102], hydrostatic pressurization[103–106], mechanical bending[107–112], and electrostriction[113], have been utilized to induce physical strain, controlling strain at the nanoscale space and exploring optical properties with nanoscale spatial resolution remain challenges.

Recently, a promising approach called tip-induced strain engineering has facilitated the application of GPa-scale pressure to specific nanoscale regions while maintaining sub-diffraction-limited spatial resolution[114–122]. By considering the simple physical definition of pressure (force divided by area), a nanoscale tip can achieve GPa-scale pressure, despite its minute force at the pN–nN level. For instance, the changing TEPL responses of a WSe_2 monolayer were demonstrated by releasing the intrinsic strain between the as-grown WSe_2 monolayer and the substrate, as shown in Fig. 4a-(i)[81]. Similar strain-induced bandgap transition was observed for a WS_2 monolayer[123]. By carefully applying local force and pressure using a plasmonic tip, the strain can be locally released in a reversible manner, resulting in the reversible changes in TEPL intensity and energy, as depicted in Fig. 4a-(ii). Moreover, confocal PL imaging before and after applying the tip-induced force and pressure revealed irreversible PL changes from the released strain, as illustrated in Fig. 4a-(iii). In addition, the nanoscale spatial resolution of TEPL spectroscopy provided detailed information about the indented region, as demonstrated in Fig. 4a-(iv). Notably, the TEPL image of the WSe_2 flake near a nucleation site (NS) region displayed initially suppressed TEPL intensity, whereas the two pressed regions exhibited distinctly blueshifted and increased TEPL signals. These findings highlight the capability of nano-mechanical tip interactions to induce both reversible and irreversible release of local strain, offering a unique approach to control the PL energy and quantum yield of nanoscale defects in 2D materials.

In a recent study performed by Koo et al., the optical properties of nanoscale wrinkles in a WSe_2 monolayer were dynamically controlled using GPa-scale pressure applied with a plasmonic tip, as depicted in Fig. 4b-(i)[28]. Figure 4b-(ii) illustrates the reversible modulation of PL intensity and energy as the tip gradually presses and releases the wrinkle structure. As the tip releases the intrinsic tensile strain on the wrinkle structure, the blueshifted PL energy is observed. At the wrinkle apex, the naturally-induced strain modifies the lattice structure, resulting in a reduced bandgap of the crystal. This reduced bandgap promotes exciton funneling into the wrinkle apex, leading to a higher PL quantum yield compared to that of the crystal face. Conversely, applying tip-pressure can release the strain at the wrinkle apex, which increases the bandgap energy and reduces exciton funneling, resulting in decreased PL intensity at the wrinkle apex. To accurately quantify the local pressure induced by the plasmonic Au tip on the WSe_2 wrinkle, a numerical simulation was performed, and the results are shown in Fig. 4b-(iii). Remarkably, the study revealed that achieving GPa scale pressure requires an extremely low level of force. Moreover, this approach allowed for dynamic engineering of the radiative decay rate from nanoscale wrinkles through systematic vertical positioning of the plasmonic Au tip, as demonstrated in Fig. 4b-(iv). Through this concept, this study showcased the switching and modulation modes of wrinkle emission using both binary pressing depths and three discrete levels. These findings highlight the unique optical characteristics of the naturally-formed nanoscale wrinkles, which differentiate them from the optical properties of the crystal face. Consequently, this work signifies the potential of nanoscale wrinkles as nanoscale light-illuminating sources in 2D semiconductors.

Furthermore, in a recent study performed by Lee et al., the combination of the tip-induced strain engineering technique with a plasmonic nanogap structure enabled dynamic control of exciton funneling and trion conversion processes, as illustrated in Fig. 4c-(i)[29]. When WSe_2 and MoS_2 monolayers were transferred onto the nanogap, the naturally generated strain gradient resulting from the suspended geometry of the crystals led to a corresponding gradient of the bandgap, with energy minima at the nanogap center. Notably, this structure is an inverse of the naturally-formed wrinkles in 2D materials. Consequently, this strain gradient caused exciton funneling in a WSe_2 monolayer and exciton-to-trion conversion in a MoS_2 monolayer, as excess electrons in n-type semiconductors funneled together with neutral excitons. Figure 4c-(ii) displays the increased trion density at the bandgap minima, obtained through TEPL spectroscopy. By gradually pressing the suspended MoS_2 monolayer on the nanogap structure, the maximum value of the strain gradient could be incrementally increased, as shown in Fig. 4c-(iii). As the tip pressed the suspended WSe_2 monolayer, the increased tensile strain leads to the increased TEPL intensity of excitons without altering the TEPL intensity of trions, as depicted in Fig. 4c-(iv). Similar tip-induced strain effect exhibiting spectral shift in a WSe_2 monolayer was also reported[124], even though tip-enhanced nano-spectroscopy measurement was not performed. By contrast, the MoS_2 monolayer exhibited a decrease in TEPL intensity of excitons along with an increase in TEPL intensity of trions, demonstrating exciton-to-trion conversion. Specifically, the gradual increase in pressure caused by the tip results in a progressive enhancement of the strain gradient, causing excitons and free electrons to be concentrated at the center of strain gradient. This increased concentration leads to the conversion of these confined excitons and free

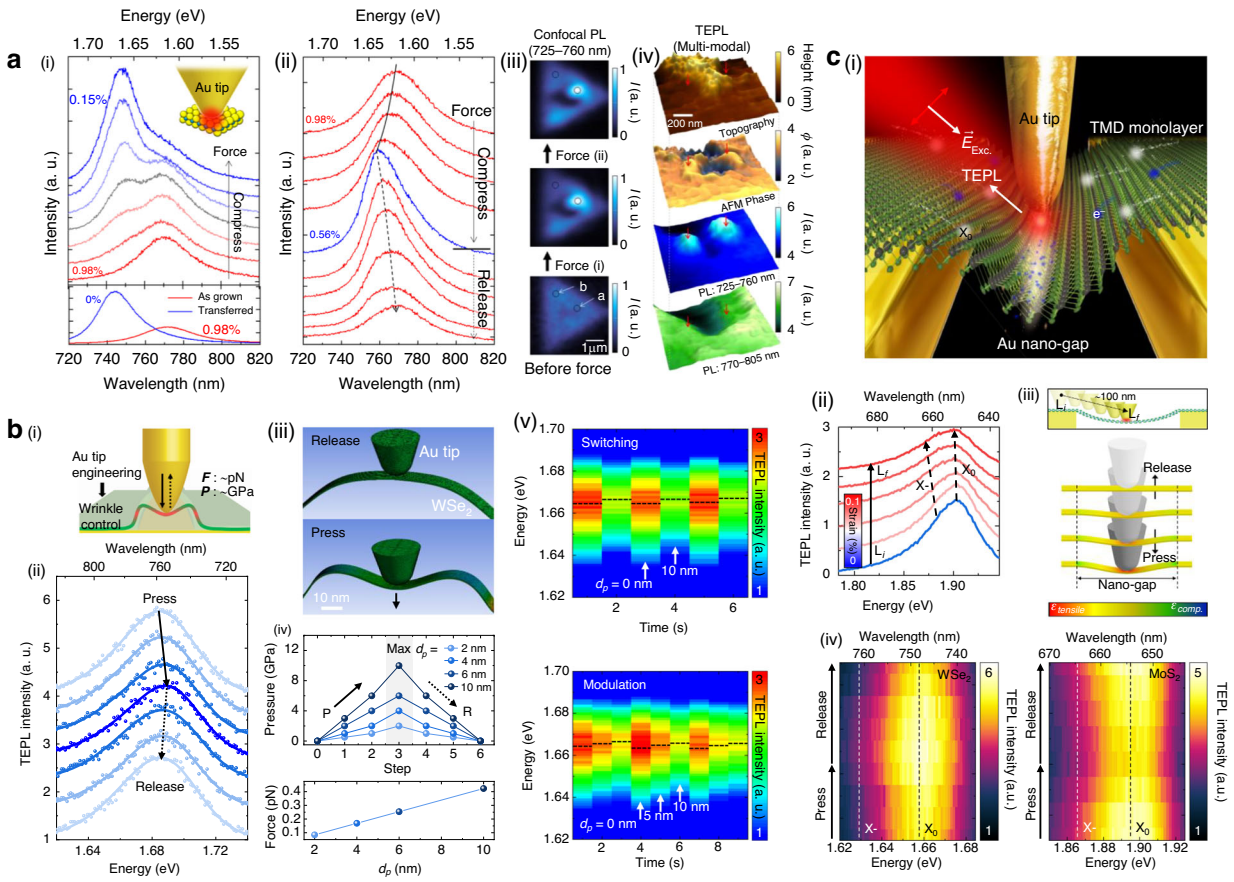

Fig. 4 Tip-induced strain engineering of TMD MLs via local pressure control. a Modifications in TEPL spectra of the as-grown WSe_2 monolayer with irreversible (i) and reversible (ii) changes of the strain on the crystal. (iii) Confocal PL images before and after releasing the irreversible (i) and reversible strain (ii). (iv) Nano-resolving of AFM topography, phase, blue shifted TEPL, and main TEPL for two strain released spots. **b** Strain engineering on the wrinkle structure in WSe_2 monolayer. (i) Schematic of tip-induced strain control on a wrinkle structure. (ii) Reversibly changing TEPL spectra with the gradual press and release of the tip. (iii) A model representing the Au tip and the WSe_2 wrinkle, designed to simulate the local pressure at the wrinkle apex caused by the tip. (iv) Computed local pressure and the force exerted on the wrinkle apex when the gold tip is pressed and released at various pressing depths ($d_p = 2$, 4, 6, and 10 nm). (v) Demonstration of switching and modulation of wrinkle TEPL by binary pressing depth and three discrete pressing depths. **c** Nanoscale strain engineering for exciton funneling and trion conversion. (i) Schematic of TMD monolayers transferred on an Au nanogap combined with TEPL spectroscopy. (ii) Simulation of strain distribution for pressured TMD monolayers on the nanogap with different tip positions. (iii) TEPL spectra of a MoS_2 monolayer as the tip moves from the edge (L_i) to the center (L_f) of the nanogap. (iv) Reversible changes in TEPL spectra of WSe_2 (left) and MoS_2 (right) monolayers by modulating tip-induced pressure. Dashed lines demonstrate the energy of excitons (black) and trions (white). **a** Reproduced with permission[81]. Copyright [2016] American Chemical Society. **b** Reproduced with permission[28]. Copyright [2021] Wiley-VCH. **c** Reproduced with permission[29]. Copyright © 2022 Lee et al., some rights reserved; exclusive licensee American Association for the Advancement of Science. No claim to original U.S. Government Works. Distributed under a Creative Commons Attribution NonCommercial License 4.0 (CC BY-NC)

electrons into trions, ultimately resulting in a reduction in the intensity of neutral excitons, while the intensity of trions increases. In this work, the spatial positioning accuracy of ~0.2 nm and GPa-scale pressure of the plasmonic Au tip allowed for precise nanoscale control of exciton dynamics in a reversible manner, including the modulation of exciton funneling rate in a WSe_2 monolayer and exciton-to-trion conversion rate in a MoS_2 monolayer. These investigations revealed subtle excitonic behaviors in nanoscale regions, while the utilization of tip-induced control modality allowed for direct and reversible regulation of these excitonic phenomena. It is important to note that the materials subject to exploration and control extend beyond the 2D TMDs discussed in this study.

The tip-induced pressure approach has opened up new avenues for investigating quantum light-matter interactions and tailoring them for various applications. In addition to nanoscale strain engineering of TMD monolayers, tip-induced strain engineering enables local modification of the lattice and electronic band structure of various low-dimensional quantum materials in a highly

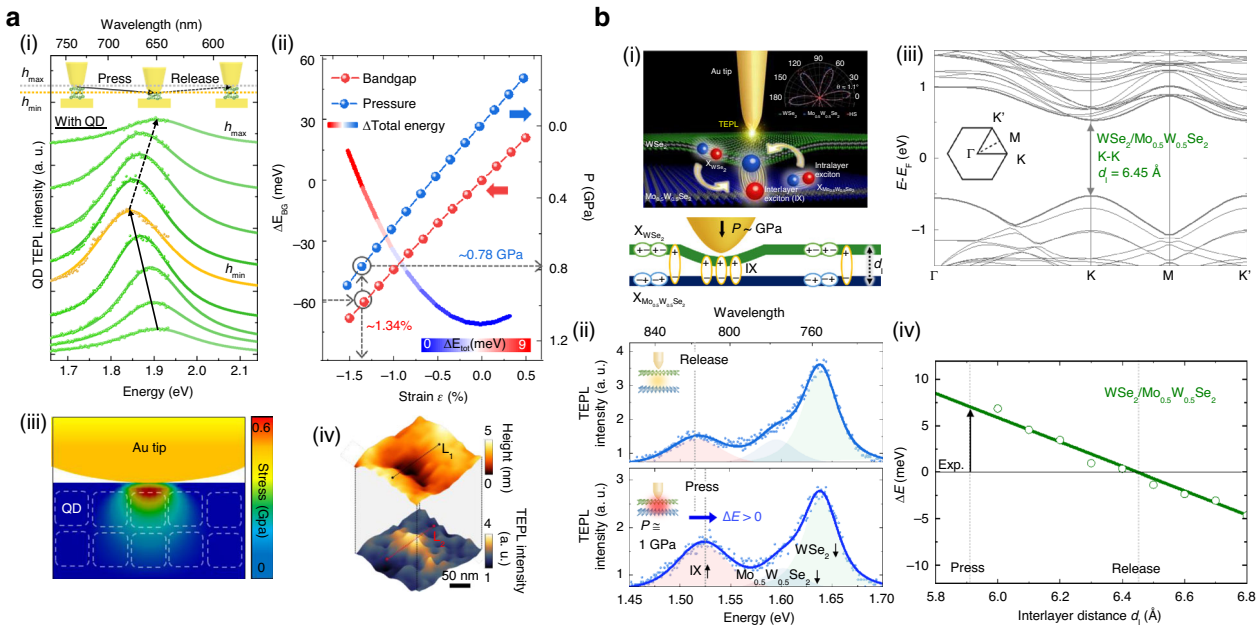

Fig. 5 Tip-induced bandgap engineering of quantum dot and 2D heterobilayer via local pressure control. a Structural and electronic band deformation of pQD ensemble. (i) Reversible tip-pressure engineering of a single pQD. (ii) Bandgap energy shift and pressure as a function of applied strain along the c-axis. The free energy graph is represented separately in the background. (iii) Numerical simulation for the distribution of stress when the Au tip applies pressure on an ensemble of pQDs. (iv) AFM image of the pQD ensemble undergoing structural modifications due to tip-pressure (top) and corresponding TEPL intensity image (bottom). **b** Local modification of interlayer coupling strength. (i) Illustrations of tip-induced control of the interlayer coupling strength for a $WSe_2/Mo_{0.5}W_{0.5}Se_2$ heterobilayer. (ii) TEPL spectra of the $WSe_2/Mo_{0.5}W_{0.5}Se_2$ heterobilayer before (top) and after (bottom) applying the tip-pressure. (iii) Electronic band structure calculated for the equilibrium interlayer distance of $d_I = 6.45$ Å. (iv) Energy shift for K-K transition as a function of interlayer distance. **a** Reprinted with permission[125]. Copyright [2021] American Chemical Society. **b** Reproduced with permission[129]. Copyright [2023] Koo et al

controlled manner. A recent study demonstrated the reversible tuning of emission energy of a single perovskite quantum dot (pQD) using GPa-scale pressure applied by a plasmonic Au tip[125]. By gradually pressing and releasing the single pQD, its emission properties can be precisely adjusted in real-time, as shown in the TEPL spectra in Fig. 5a-(i). Density functional theory (DFT) calculations quantified the applied strain of ~1.34% and the pressure of ~0.78 GPa required to achieve the experimentally obtained energy shift in PL spectra, as shown in Fig. 5a-(ii). In the case of the pQD ensemble, applying tip-pressure beyond a certain threshold leads to permanent modifications in their structural and radiative emitting properties, as depicted in Fig. 5a-(iii), (iv). The affected area in the ensemble exhibited structural deformation, accompanied by an increase in TEPL intensity. This alteration in PL intensity can be attributed to the reduced distance between neighboring pQDs, as they were compressed by the applied pressure. It decreased the plasmonic cavity mode volume between the tip and Au substrate, as shown in the correlation between the topography and TEPL images of Fig. 5a-(iii), (iv). The proposed tip-pressure engineering technique offered a unique approach to modulate the optical and electronic properties of perovskites at the single QD level. Furthermore, this study demonstrated that the plasmonic cavity formed underneath the plasmonic Au tip with the Au substrate suppresses the increased nonradiative decay rate from structural deformation, thereby preserving radiative properties even in the highly pressed regime. As another direction of applications, the ability to induce a phase transition by tip-pressure could have far-reaching implications in material sciences and the development of advanced nanoscale manipulation technologies for phase-transition materials, such as perovskite compounds[126], topological insulators[127], and high temperature superconductors[128]. It should be also noted that the demonstrated work confirmed the consistent results of the tip-pressure experiment when using different tips. This approach was also applied to TMD heterostructures to tune the PL energy of interlayer excitons. Figure 5b-(i) presented a conceptual illustration of nanoscale pressure engineering of a TMD heterobilayer using a plasmonic tip[129]. When the Au tip applies pressure onto a $WSe_2/Mo_{0.5}W_{0.5}Se_2$ heterobilayer, the interlayer distance becomes smaller, leading to an increase in interlayer coupling strength. Consequently, this effect leads to an increased PL intensity of interlayer excitons with a

simultaneous decrease in the PL intensity of intralayer excitons, as shown in Fig. 5b-(ii). Furthermore, for local regions that already have a high interlayer coupling strength, the GPa-scale tip-pressure could induce bandgap and PL energy shifts in the heterobilayer due to modifications in the lattice structure. Figure 5b-(iii) exhibited DFT calculations showing an equilibrium interlayer distance of 6.45 Å for the untreated WSe_2/$Mo_{0.5}W_{0.5}Se_2$ heterobilayer. As demonstrated in Fig. 5b-(iv), reducing the interlayer distance resulted in an increased emission energy of the interlayer excitons. Therefore, the experimentally reduced interlayer distance could be estimated by monitoring the TEPL energy of interlayer excitons. Taking into account the distinctive characteristics of interlayer excitons, including extended valley polarization, coherence, and recombination times, this method establishes a foundation for local manipulation of interlayer excitons. This can potentially be extended to nano-integrated excitonic/trionic circuits and advanced optoelectronic devices in subsequent generations.

In this section, we have reviewed the recent developments and progress of the tip-induced pressure engineering approach applied to various low-dimensional quantum materials. For effective harnessing of nanoscale modifications in lattice structure, changes in bandgap and PL response, and a diverse range of quantum light-matter interactions, the ability to probe nanoscale optical phenomena is an indispensable prerequisite. When combined with TEPL spectroscopy, the demonstrated tip-induced GPa-pressure engineering approaches not only provide a comprehensive correlated analysis of the structural and optical properties of various materials but also offer a practical means for modifying mechanical and electronic properties at the desired nanoscale region. In addition, the effect of tip-induced pressure in the strong coupling regime has not been yet clarified due to the lack of suitable experimental approaches. We expect that the tip-induced GPa scale pressure-engineering technique could potentially open a pathway to investigate pressure-related optical phenomena in the strong coupling regime. It should be noted that since the Au tip is composed of a relatively soft metal, it is important to consider the potential structural modifications that may occur during tip-pressure experiments. In previous studies we have referenced, the experiments primarily focused on soft materials, such as nano-wrinkles in 2D materials, suspended 2D sheets on nanogaps, and perovskite QDs. This choice of materials aimed to minimize structural deformation of the Au tip. As a forward-looking perspective, we believe it would be beneficial to explore the fabrication of Au alloy tips with higher hardness. This approach has the potential to enhance the versatility and applicability of tip-pressure experiments, enabling investigations across a broader range of materials and systems.

Tip-induced control of near-field polarization at the nanoscale

Polarization control of light in the far-field regime has been extensively investigated and applied for optical characterization and manipulation of light-matter interactions in photonic, plasmonic, and optoelectronic systems[130–138]. For instance, this approach can reveal the molecular or crystal orientation[139–141], electronic band structures of low-dimensional semiconductors[142–145], and light-matter coupling in hetero- and hybrid structures[146–149]. Likewise, polarization control in the near-field regime is also highly desired for studying nanoscale characteristics, i.e., coupled behavior of single quantum emitters[150–152] and excitonic states in superlattice structures[153–155]. Yet, modulation of near-field polarization at the nanoscale remains challenging. Conventional tip-enhanced nano-spectroscopy is known to suffer from limited tunability of polarization at the tip apex since traditionally used plasmonic tips generate strong out-of-plane fields at the apex, while the corresponding in-plane fields are relatively weak[25]. Controlling optical field distribution at the tip apex can therefore increase sensitivity and enhance light-matter interaction with in-plane oriented dipole excitations, such as excitons in 2D materials[156].

One approach to create substantial in-plane components in a conventional conical tip structure is by using a simple geometry modification, as shown in Fig. 6a-(i), (ii). Adjusting the angle of the tip axis with respect to the substrate under side illumination significantly increases the in-plane field component at the tip apex[157], which is attributed to the geometry-dependent damping of the collective oscillations of electrons[158]. The electron oscillations are overdamped for a vertically aligned tip due to the semi-infinite geometry with only a single metal–dielectric interface, resulting in a weak localized surface plasmon resonance (LSPR). On the other hand, the collective electron oscillations for a tilted tip are confined within a finite volume near the apex, leading to an enhanced LSPR response for both the in-plane and out-of-plane components compared to the vertically aligned tip. The angle-dependent in-plane enhancement of the tilted tip is clearly demonstrated in the imaging of ferroelectric domains in single-crystalline $YMnO_3$, as shown in Fig. 6a-(iii), (iv)[159,160]. When the tip is tilted at 35° to the sample plane, a distinct contrast between domains is observed in the tip-enhanced second harmonic generation (SHG) image, while the domains are barely noticeable when the tip is oriented vertically ($\theta_{tip} = 90°$). To systematically evaluate the field enhancement of the tilted tip, the authors calculated nanoscale spatial distributions of the in-plane $|E_x|^2$ and out-of-plane $|E_z|^2$ components of the optical field for a variable tip tilting angle. The results shown in Fig. 6a-(v), (vi) demonstrate

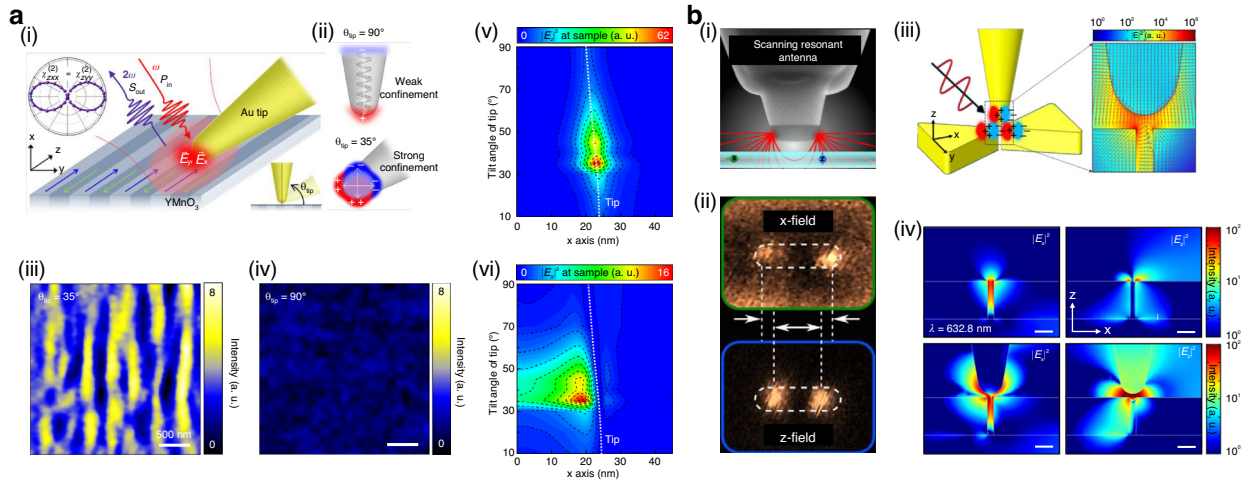

Fig. 6 Tip-induced nearfield polarization control by exploiting plasmonic cavity geometry. a Near-field polarization control by tilting the conventional antenna tip. (i) Schematic of *x*-cut single-crystalline $YMnO_3$ nano-crystallographic imaging using the tilted tip. (ii) Illustration of the geometric confinement for collective electron oscillations in conventional tip oriented at 90° (top) to the sample surface (top) and tilted tip oriented at 35° (bottom). Tip-enhanced SHG images measured with tips tilted at an angle of 35° (iii) and at 90° (iv). Calculations for the in-plane (v) and out-of-plane (vi) optical field intensities at the sample for varying tilt angle of the tip (θ_{tip}). **b** Designed nanoantenna structures to manipulate the near-field polarization. (i) Schematic of scanning single molecule emitters using a special resonant dipole nanoantenna. (ii) Measured *x*- and *z*-field intensity from the selected individual molecules with *x*- and *z*-oriented dipole moments. (iii) Schematic of vector field polarization in a triple-tips nanostructure, which consists of a bowtie antenna structure and a tip (left), together with FDTD simulation result of plasmonic field enhancement in the triple-tips nanostructure (right). (iv) Calculated in-plane ($|E_x|^2$, left) and out-of-plane ($|E_z|^2$, right) field distributions of the bowtie structure without (top) and with (bottom) a vertically oriented tip. Reprinted with permission from ref. [157]. Copyright [2018] American Chemical Society. **b**-(i), (ii) Reproduced with permission[162]. Copyright [2014] American Chemical Society. **b**-(iii), (iv) Reproduced with permission[165]. Copyright [2021] John Wiley and Sons

that both the in-plane and out-of-plane field components are maximized at the angle of 35°. Thus, through the experimental geometry of tip-enhanced nano-spectroscopy, one can substantially modify the near-field distribution and improve light-matter interactions between the tip and excitations in the studied sample.

Another approach to manipulating the near-field polarization in tip-enhanced nano-spectroscopy takes advantage of the geometry-dependent field distribution in plasmonic nano-antennas[161]. For example, the use of a resonant dipole antenna instead of a conventional tip has been demonstrated, as shown in Fig. 6b-(i)[33,162]. To produce the resonant antenna, a fiber tip was tapered using the heat pulling method, which is generally used for near-field scanning optical microscopy (NSOM), followed by Al deposition and focused ion beam (FIB) milling to fabricate a rectangular antenna with the dimensions of 200 nm × 60 nm. The fabricated rectangular structure provides spatially separated in-plane and out-of-plane field distributions in the tip-sample gap. Therefore, when raster scanned over a sample containing single molecules, the antenna structure allows extracting information on the dipole orientational of each molecule, as shown in Fig. 6b-(ii)[163,164].

Instead of modifying the tip geometry, combining a conventional tip with additional plasmonic nanostructures has also been suggested as a way to modulate the near-field distribution. For example, a triple-sharp-tips structure has been proposed and demonstrated by integrating a bowtie antenna and a conventional tip, as shown in Fig. 6b-(iii)[165]. To study the spatial distribution of the in-plane and out-of-plane field components for such structure, optical field distribution has been calculated for a bowtie structure with and without the tip using finite-difference time-domain (FDTD) simulations, as shown in Fig. 6b-(iv). The results showed that the bowtie structure without the tip has a strong in-plane field component ($|E_x|^2$, top left panel) inside the gap while the corresponding out-of-plane field ($|E_z|^2$, top right panel) is significantly weaker. In contrast, the triple-sharp-tips structure formed in the presence of the tip exhibits a significant enhancement of both E_x and E_z fields at the bowtie cavity (bottom left and right panels, respectively). The authors further utilized the structure to induce and investigate localized excitons in a WSe_2 monolayer. Due to the strain of the transferred WSe_2 on the bowtie structure[166] and strong field enhancement at the cavity, localized excitons at room temperature were observed at the cavity of the triple-sharp-tips structure[162].

All approaches to control the near-field polarization reviewed in this section so far relied on modifying the geometry and structure of plasmonic tips. While these

approaches in principle allowed one to manipulate the field distribution at the tip and enhance light-matter interaction for dipole moments oriented in-plane, which is difficult to achieve with conventional tip-enhanced nano-spectroscopy, the requirement for a special experimental configuration limits their potential applications. This calls for a more versatile method for controlling the near-field polarization.

To address the aforementioned issue, optically controlled adaptive tip-enhanced nano-spectroscopy was demonstrated using wavefront shaping method, as shown in Fig. 7[167,168]. A spatial light modulator (SLM) integrated into a conventional tip-enhanced nano-spectroscopy setup allows manipulating the phase of incident light by dividing the laser beam into multiple segments and controlling the phase of each segment[169–171]. The SLM-shaped wavefront is then used to illuminate the tip-sample gap, and the target signal of the detected TEPL response is optimized using the sequential feedback algorithm, as shown in Fig. 7a-(ii). To understand the effect of SLM on the near-field polarization, the phase-dependent field enhancement at the tip is evaluated theoretically via FDTD simulations, with the results shown in Fig. 7b-(i), (ii). To examine the local field enhancement with respect to spatial phase difference, the incident light source was constructed with many optical sources, all with the same linear polarization but varying phase delays ranging from 0 to π. Both in-plane (1) and out-of-plane (2) near-field components were found to be sensitive to phase delay, which indicates that adjusting the phase delay provides accurate control on the local field enhancement and associated light-matter interactions. The calculated phase-dependent near-field polarization behavior was confirmed experimentally via measuring excitonic TEPL signals from a WSe_2 monolayer sample. As depicted in Fig. 7c-(i), the PL intensity generated with a radially polarized excitation beam in the monolayer (black) is first considerably increased as the tip approached the sample (TEPL, blue), which is attributed to the conventional tip enhancement effect. The TEPL intensity is further enhanced by the adaptive optimization of the excitation wavefront with SLM (*a*-TEPL, red), more than twice compared to the conventional TEPL intensity, with the corresponding enhancement factor of $\sim 4.4 \times 10^4$, which is attributed to the stronger in-plane enhancement at the tip.

In addition, adaptive TERS (*a*-TERS) experiment was carried out on the same sample to analyze the effects of wavefront shaping on Raman responses as the vibrational modes have different orientation and enhancement mechanism. Figure 7c-(ii) shows the far-field Raman (black) and TERS spectra of a WSe_2 monolayer, both with (red) and without (blue) wavefront shaping. The *a*-TERS intensities of A(M) (asymmetric phonon mode at the M point) and $A_{1g} + E^1_{2g}$ (out-of-plane vibration of Se atoms and in-plane vibration of W and Se atoms) modes were enhanced more than two times in comparison to the TERS signals in the absence of wavefront shaping, while the E_{1g} (in-plane vibration of Se atoms) mode was slightly decreased. This result indicates that the phase mask optimization procedure enhances the vibrational modes in the out-of-plane direction (A_{1g}), but not the in-plane modes (E_{1g}) [172,173]. The authors also point out that the additional enhancement by the wavefront shaping varies between different tips (1.3 ~ 2.5 times compared to normal TERS/TEPL), which is attribute to the nanoscale differences in the tip apex geometry. If the fabrication of identical tip shapes is feasible, it will enable the quantitative analysis of enhancement and field distribution.

In addition to the orientation-dependent enhancement of vibrational modes in *a*-TERS, selective enhancement of PL spectra for excitons with different dipole orientations has been demonstrated in a $WSe_2/Mo_{0.5}W_{0.5}Se_2$ heterostructure, as shown in Fig. 7d-(i), (ii)[168]. In the heterostructure, *a*-TEPL can selectively enhance intralayer excitons X_{WSe_2} (in-plane dipole orientation) and interlayer excitons IX (out-of-plane dipole orientation) using different phase masks. The mechanism behind the selective control of two PL peaks relies on two aspects, namely, the different spatial distribution of excitons created for different phase masks and distinctive dependencies of radiative emission on in-plane coordinate for intra- and inter-layer excitons. As shown in Fig. 7d-(iii), the simulated spatial distributions of the exciton density are qualitatively different for two model phase masks corresponding to the in-plane (PM1, gray) and out-of-plane (PM2, red) polarized incident light. In addition, the Purcell factors calculated for horizontally (P_H) and vertically (P_V) oriented dipoles exhibit distinctly different dependencies on the in-plane exciton coordinate, corresponding to different radiative emission rates of X_{WSe_2} and IX, as shown in Fig. 7d-(iv). The total *a*-TEPL response is then evaluated as a convolution of the spatial dependencies for the exciton density and Purcell factor, which yields selective enhancement of X or IX peaks for different phase mask, in agreement with the experimental results. Based on the demonstrated selective modulation of X and IX PL peaks, the authors proposed a conceptual device, an optically controlled nano-excitonic transistor. As shown in Fig. 7e, the proposed device can controllably generate two optical bits of data at the nanoscale. A 2-ternary digit (trit) system can be also developed based on the same idea, where the *a*-TEPL intensities of X_{WSe_2} and IX can be controlled to represent −1, 0, and 1 digits. Furthermore, since the demonstrated approach has few-nm spatial resolution, it allows developing data storage and processing elements with data capacity exceeding that of a Blu-ray disc by more than 1000 times, as depicted in Fig. 7f. In addition, we envision that the near-field

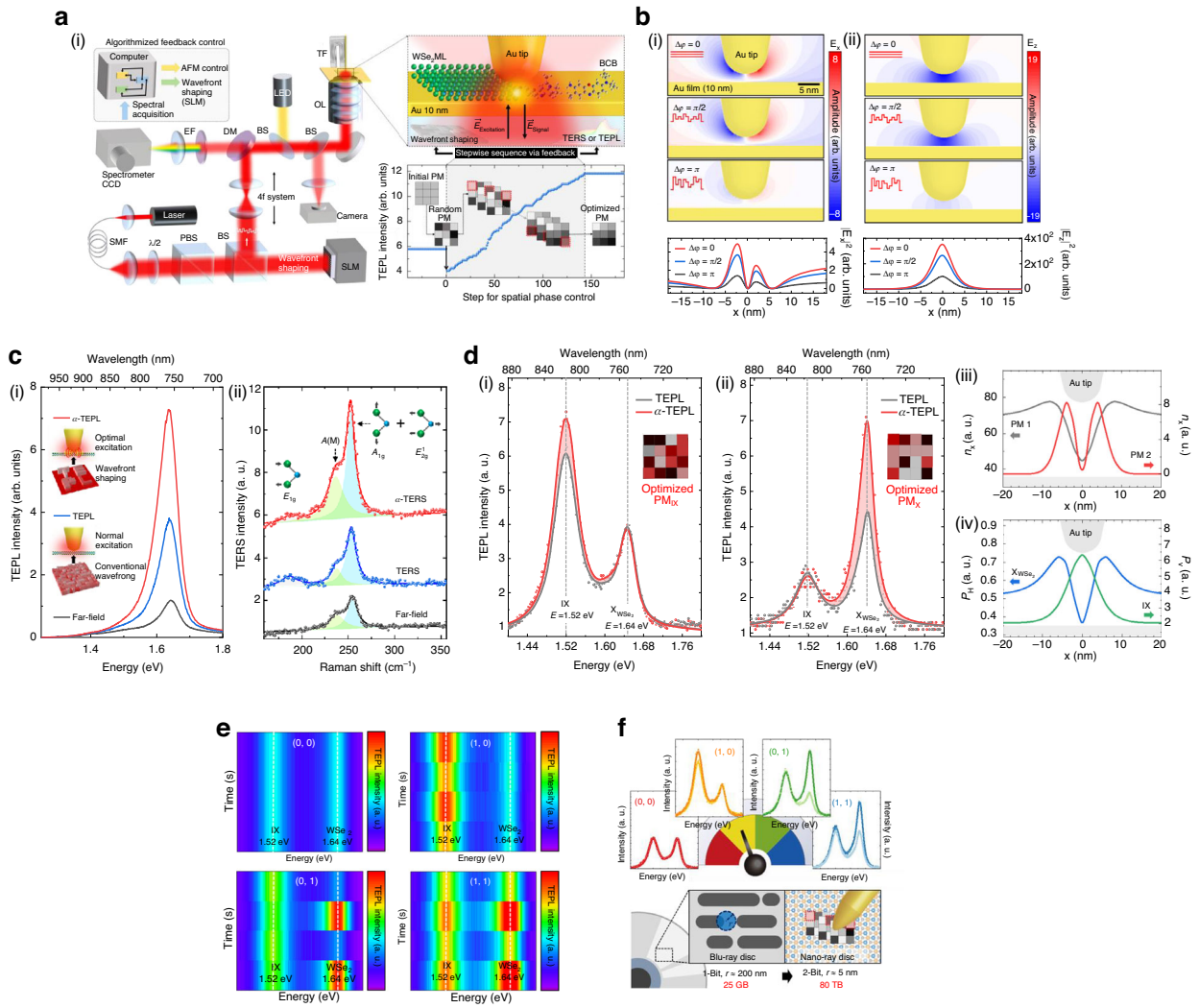

Fig. 7 Tip-induced nearfield polarization control by optical phase modulation. a Dynamic wavefront shaping method with tip-enhanced nano-spectroscopy. (i) Schematic diagram of the experimental setup for adaptive tip-enhanced nano-spectroscopy. A He-Ne laser with a wavelength of 632.8 nm is spatially filtered and expanded to fully illuminate the active area of a spatial light modulator (SLM) for wavefront shaping. The wavefront-shaped beam is then imaged onto the back aperture of an objective lens (OL) within a 4f system, enabling dynamic manipulation of LSPR at the tip. (ii) TEPL intensity of a WSe_2 monolayer changes as the phase mask (PM) is optimized using a stepwise sequential algorithm. The TEPL response with the optimal phase mask shows stronger enhancement than the conventional TEPL setup. **b** Simulated optical field distributions at the tip-sample gap for different phase masks. (i), (ii) In-plane ($|E_x|^2$) and out-of-plane ($|E_z|^2$) components of the optical field with respect to spatial phase variation. Intensity profiles of the in-plane ($|E_x|^2$) and out-of-plane ($|E_z|^2$) optical field at a horizontal plane 1 nm below the tip (bottom). **c** (i), (ii) Far-field PL/Raman spectrum (black) and TEPL/TERS spectra of a WSe_2 monolayer without SLM (blue) and with optimal wavefront conditions using SLM (*a*-TEPL, red). **d** Selective TEPL modulation of intra- and interlayer exciton emission in a $WSe_2/Mo_{0.5}W_{0.5}Se_2$ heterobilayer via wavefront shaping. (i) Comparison of normal TEPL and *a*-TEPL spectra without (gray) and with (red) the optimized phase mask for the IX peak (PM_{IX}). (ii) Comparison between normal TEPL and *a*-TEPL spectra without (gray) and with (red) the optimized phase mask for the X_{WSe_2} peak (PM_X). (iii) Simulated exciton density (n_x) profiles of WSe_2 intralayer excitons (X_{WSe_2}) along the *x*-axis for two different model phase masks (PM1 and PM2). (iv) Simulated Purcell factors for the in-plane (X_{WSe_2}, P_H) and out-of-plane (IX, P_V) dipoles as functions of the dipole position with respect to the tip. **e** Demonstration of optical switching in *a* nano-excitonic transistor using *a*-TEPL spectra of IX and X_{WSe_2}. These figures demonstrated data units of (0, 0), (1, 0), (0, 1), and (1, 1) for the operation of a 2-bit nano-excitonic transistor. **f** Representation of two-optical bit processing using the four distinct data units from (**e**) and comparison of the nano-ray disc utilizing a 2-bit nano-excitonic transistor, which has significantly higher data density and capacity, with a traditional Blu-ray disc. **a** Reproduced with permission[167]. Copyright [2021] Lee. **b** Reproduced with permission[167]. Copyright [2021] Lee. **c** Reproduced with permission[167]. Copyright [2021] Lee. **d** Reproduced with permission[168]. Copyright [2023] American Chemical Society. **e** Reproduced with permission[168]. Copyright [2023] American Chemical Society. **f** Reproduced with permission[168]. Copyright [2023] American Chemical Society

polarization control at the tip can further expand to light-matter interactions in the ultrafast time domain[174,175]. Notably, fs-pulsed laser excitation at plasmonic tips has been shown to reveal the nanoscale nonlinear optical phenomena in 2D van der Waals materials[176,177]. Furthermore, recent advancements in ultrafast spatio-temporal light control, utilizing active metasurfaces[178] and SLM[179], enable ultrafast wavefront manipulation with potential applications in near-field polarization control at the tip in both time and space domains.

In summary, this section provides an overview of the methods to control near-field polarization for enhancing tip-induced light-matter interactions. Strong in-plane enhancement can be enabled by modifying the geometry and structure of the tip, i.e., tilting a conventional tip, fabricating a resonant antenna at the tip end, and integrating a conventional tip with additional nanostructures. Adaptive wavefront shaping using SLM is suggested as a more versatile approach that enables selective enhancement and suppression of the desired optical responses in a conventional tip-enhanced nano-spectroscopy scheme without the need for modification of the tip structure. Given that this technique is still in its nascent stages, there is a pressing need for more comprehensive and systematic experiments aimed at characterizing the near-field polarization induced by wavefront shaping. These dedicated efforts are poised to advance our comprehension of adaptive near-field optics, paving the way for a multitude of potential applications and expanded capabilities. The ability to control near-field polarization introduces a new degree of freedom for dynamic all-optical control of low-dimensional quantum materials, which will facilitate the development of novel compact photonic and optoelectronic devices for processing classical and quantum information.

Conclusions

In this comprehensive review, we have delved into the recent advancements in tip-induced control of quantum light-matter interactions at the nanoscale, with a particular focus on its applications in low-dimensional quantum materials. Going beyond the conventional uses of SPM[180,181] and tip-enhanced nano-spectroscopy[20] to overcome optical diffraction limits and improve sensitivity, we explored how incorporating newly developed control functions enables the manipulation of tip-enhanced spectroscopy to precisely influence light-matter interactions at the nanoscale.

Throughout the review, we highlighted three unique approaches for controlling nanoscale light-matter interactions. Firstly, we discussed the tip-induced control of radiative emission via cavity-gap regulation. By carefully adjusting the distance between the tip and the sample with sub-nanometer precision in ambient conditions, researchers demonstrated that the mode volume of the tip-cavity can be dynamically engineered, allowing us to control the radiative decay rate of emitters positioned within the cavity. The controllable tip-cavity mode volume significantly changes the field enhancement and Purcell factor, which in turn modifies the radiative emitting properties of low-dimensional quantum materials, such as dark exciton emission[25,182,183] and the coupling strength between the cavity and emitters[31,33,184,185].

Secondly, we explored the emerging field of tip-induced control of excitonic behaviors through GPa-scale pressure engineering. In addition to traditional tip indentation methods[186,187], we showed how combining this approach with tip-enhanced nano-spectroscopy allows us to modify the mechanical and electronic properties of specific nanoscale regions while investigating the structural and optical properties of low-dimensional quantum materials, such as TMD mono- and bi-layers and perovskite QDs.

Lastly, we examined the promising avenue of tip-induced near-field polarization controls and their wide-ranging applications. Traditionally, physical modifications to the tip, such as the tilted-tip method and the fabrication of plasmonic structures, were employed to change the direction of near-field polarization. However, recent advances in adaptive optics techniques have provided more versatile and generalizable approaches, even with normal plasmonic tips. By reconstructing the wavefront of the excitation beam using SLM, researchers demonstrated the ability to achieve arbitrary near-field polarization states at the tip apex. This all-optical near-field polarization control technique selectively enhances or suppresses quantum light-matter interactions, opening up possibilities for various optoelectronic device applications.

In addition to the demonstrated tip-induced control approaches, numerous other methods can be combined with tip-enhanced nano-spectroscopy. For instance, magnetic field or force from magnetized tips can manipulate light-matter interactions by tuning the magneto-optical resonance for various systems[188,189]. Likewise, conductive tips can provide an additional modulation parameter through the local electric field, influencing plasmonic and electronic systems[190,191]. Furthermore, different approaches can be employed together to manipulate tip-induced light-matter interactions in a hybrid manner, for example, tip-induced hot electron injection into a TMD heterobilayer with modifications to the tip-cavity gap[126].

In this review, while our discussions mainly focused on the optical phenomena in the visible and near-infrared (NIR) range, the tip-induced control approaches can also be applied to ultraviolet (UV)[192,193], infrared (IR)[194,195], and even Terahertz range[196,197]. Additionally, the tip-induced control approaches can be extended to chemical and biological systems, allowing manipulation of

molecular dynamics at the single-molecule level[43,198] and influencing photosynthesis in biological materials[199,200].

In conclusion, this review showcases the exciting progress in tip-induced control of quantum light-matter interactions at the nanoscale, particularly in the realm of low-dimensional quantum materials. These novel approaches, including cavity-gap control, GPa-scale pressure engineering, and all-optical near-field polarization control, offer promising opportunities for tailoring and manipulating light-matter interactions in nanoscale systems. The insights presented here contribute to advancing the field of nanophotonics and lay the foundation for the development of cutting-edge optoelectronic devices with unprecedented capabilities.

Acknowledgements

This work was supported by the projects of 2020R1C1C101130114, 2022M3H4A1A0409639611, SSTP-BA2102-05, RS-2022-00164799, 2023-22030003-30, 2021R1A6A1A1004294413, 2019-0-00005, and RS-2023-00258359. V.K. acknowledges support from Priority 2030 Federal Academic Leadership Program.

Author contributions

Y.K., T.M., M.K., H.J., C.L., H.L., V.K., and K.-D.P. wrote the manuscript. K.-D.P. supervised this work.

Conflict of interest

The authors declare no competing interests.

Received: 28 August 2023 Revised: 26 November 2023 Accepted: 10 January 2024
Published online: 25 January 2024

References

1. Fang, J. Z. et al. Recent advances in low-dimensional semiconductor nanomaterials and their applications in high-performance photodetectors. *InfoMat* **2**, 291–317 (2020).
2. Zhang, L. et al. High-performance quasi-2D perovskite light-emitting diodes: from materials to devices. *Light Sci. Appl.* **10**, 61 (2021).
3. Wang, Y. H., Nie, Z. H. & Wang, F. Q. Modulation of photocarrier relaxation dynamics in two-dimensional semiconductors. *Light Sci. Appl.* **9**, 192 (2020).
4. Chen, J. H. et al. Silica optical fiber integrated with two-dimensional materials: towards opto-electro-mechanical technology. *Light Sci. Appl.* **10**, 78 (2021).
5. Takagahara, T. & Takeda, K. Theory of the quantum confinement effect on excitons in quantum dots of indirect-gap materials. *Phys. Rev. B* **46**, 15578 (1992).
6. Latini, S., Olsen, T. & Thygesen, K. S. Excitons in van der Waals heterostructures: the important role of dielectric screening. *Phys. Rev. B* **92**, 245123 (2015).
7. Butler, S. Z. et al. Progress, challenges, and opportunities in two-dimensional materials beyond graphene. *ACS Nano* **7**, 2898–2926 (2013).
8. Geim, A. K. Graphene: status and prospects. *Science* **324**, 1530–1534 (2009).
9. Shen, H. B. et al. Visible quantum dot light-emitting diodes with simultaneous high brightness and efficiency. *Nat. Photonics* **13**, 192–197 (2019).
10. Lorchat, E. et al. Filtering the photoluminescence spectra of atomically thin semiconductors with graphene. *Nat. Nanotechnol.* **15**, 283–288 (2020).
11. Mehdi Pour, M. et al. Laterally extended atomically precise graphene nanoribbons with improved electrical conductivity for efficient gas sensing. *Nat. Commun.* **8**, 820 (2017).
12. Huang, X. et al. A two-dimensional π–d conjugated coordination polymer with extremely high electrical conductivity and ambipolar transport behaviour. *Nat. Commun.* **6**, 7408 (2015).
13. Jo, S. et al. Negative differential capacitance in ultrathin ferroelectric hafnia. *Nat. Electron.* **6**, 390–397 (2023).
14. Ghatge, M. et al. An ultrathin integrated nanoelectromechanical transducer based on hafnium zirconium oxide. *Nat. Electron.* **2**, 506–512 (2019).
15. Odom, T. W. et al. Atomic structure and electronic properties of single-walled carbon nanotubes. *Nature* **391**, 62–64 (1998).
16. Addou, R., Colombo, L. & Wallace, R. M. Surface defects on natural MoS_2. *ACS Appl. Mater. Interfaces* **7**, 11921–11929 (2015).
17. Kirmse, H. et al. Transmission electron microscopy investigation of structural properties of self-assembled CdSe/ZnSe quantum dots. *Appl. Phys. Lett.* **72**, 1329–1331 (1998).
18. Liu, H. J. et al. Molecular-beam epitaxy of monolayer and bilayer WSe_2: a scanning tunneling microscopy/spectroscopy study and deduction of exciton binding energy. *2D Mater.* **2**, 034004 (2015).
19. Xu, K., Cao, P. G. & Heath, J. R. Scanning tunneling microscopy characterization of the electrical properties of wrinkles in exfoliated graphene monolayers. *Nano Lett.* **9**, 4446–4451 (2009).
20. Stöckle, R. M. et al. Nanoscale chemical analysis by tip-enhanced Raman spectroscopy. *Chem. Phys. Lett.* **318**, 131–136 (2000).
21. Park, K. D. et al. Probing bilayer grain boundaries in large-area graphene with tip-enhanced Raman spectroscopy. *Adv. Mater.* **29**, 1603601 (2017).
22. Lee, H. et al. Tip-enhanced photoluminescence nano-spectroscopy and nano-imaging. *Nanophotonics* **9**, 3089–3110 (2020).
23. Bouhelier, A. et al. Plasmon-coupled tip-enhanced near-field optical microscopy. *J. Microsc.* **210**, 220–224 (2003).
24. Guzatov, D. V. & Klimov, V. V. Optical properties of a plasmonic nano-antenna: an analytical approach. *New J. Phys.* **13**, 053034 (2011).
25. Park, K. D. et al. Radiative control of dark excitons at room temperature by nano-optical antenna-tip Purcell effect. *Nat. Nanotechnol.* **13**, 59–64 (2018).
26. Hasz, K. et al. Tip-enhanced dark exciton nanoimaging and local strain control in monolayer WSe_2. *Nano Lett.* **23**, 198–204 (2023).
27. Zhou, J. Z. et al. Near-field coupling with a nanoimprinted probe for dark exciton nanoimaging in monolayer WSe_2. *Nano Lett.* **23**, 4901–4907 (2023).
28. Koo, Y. et al. Tip-induced nano-engineering of strain, bandgap, and exciton funneling in 2D semiconductors. *Adv. Mater.* **33**, 2008234 (2021).
29. Lee, H. et al. Drift-dominant exciton funneling and trion conversion in 2D semiconductors on the nanogap. *Sci. Adv.* **8**, eabm5236 (2022).
30. Shao, J. Q. et al. Probing nanoscale exciton funneling at wrinkles of twisted bilayer MoS_2 using tip-enhanced photoluminescence microscopy. *J. Phys. Chem. Lett.* **13**, 3304–3309 (2022).
31. Park, K. D. et al. Tip-enhanced strong coupling spectroscopy, imaging, and control of a single quantum emitter. *Sci. Adv.* **5**, eaav5931 (2019).
32. May, M. A. et al. Nano-Cavity QED with tunable nano-tip interaction. *Adv. Quantum Technol.* **3**, 1900087 (2020).
33. Groß, H. et al. Near-field strong coupling of single quantum dots. *Sci. Adv.* **4**, eaar4906 (2018).
34. Maryam, W. et al. Dynamics of a vertical cavity quantum cascade phonon laser structure. *Nat. Commun.* **4**, 2184 (2013).
35. Higashitarumizu, N. et al. Long operating lifetime mid-infrared LEDs based on black phosphorus. *Nat. Commun.* **14**, 4845 (2023).
36. Istrati, D. et al. Sequential generation of linear cluster states from a single photon emitter. *Nat. Commun.* **11**, 5501 (2020).
37. Gao, Y. et al. Photon-trapping microstructures enable high-speed high-efficiency silicon photodiodes. *Nat. Photonics* **11**, 301–308 (2017).
38. Li, W. B. et al. Light-activated interlayer contraction in two-dimensional perovskites for high-efficiency solar cells. *Nat. Nanotechnol.* **17**, 45–52 (2022).
39. Huang, S. X. et al. Ultrasmall mode volumes in plasmonic cavities of nanoparticle-on-mirror structures. *Small* **12**, 5190–5199 (2016).
40. Jakob, L. A. et al. Giant optomechanical spring effect in plasmonic nano-and picocavities probed by surface-enhanced Raman scattering. *Nat. Commun.* **14**, 3291 (2023).
41. Chen, W. et al. Probing the limits of plasmonic enhancement using a two-dimensional atomic crystal probe. *Light Sci. Appl.* **7**, 56 (2018).
42. Kleemann, M. E. et al. Strong-coupling of WSe_2 in ultra-compact plasmonic nanocavities at room temperature. *Nat. Commun.* **8**, 1296 (2017).
43. Chikkaraddy, R. et al. Single-molecule strong coupling at room temperature in plasmonic nanocavities. *Nature* **535**, 127–130 (2016).
44. Zhang, C. et al. Switching plasmonic nanogaps between classical and quantum regimes with supramolecular interactions. *Sci. Adv.* **8**, eabj9752 (2022).
45. Kinkhabwala, A. et al. Large single-molecule fluorescence enhancements produced by a bowtie nanoantenna. *Nat. Photonics* **3**, 654–657 (2009).

46. Chen, X. D. et al. Focusing the electromagnetic field to $10^{-6}\lambda$ for ultra-high enhancement of field-matter interaction. *Nat. Commun.* **12**, 6389 (2021).
47. Bitton, O. et al. Vacuum Rabi splitting of a dark plasmonic cavity mode revealed by fast electrons. *Nat. Commun.* **11**, 487 (2020).
48. Luo, Y. et al. Purcell-enhanced quantum yield from carbon nanotube excitons coupled to plasmonic nanocavities. *Nat. Commun.* **8**, 1413 (2017).
49. Gupta, S. N. et al. Complex plasmon-exciton dynamics revealed through quantum dot light emission in a nanocavity. *Nat. Commun.* **12**, 1310 (2021).
50. Hu, S. R. et al. Experimental realization of deep-subwavelength confinement in dielectric optical resonators. *Sci. Adv.* **4**, eaat2355 (2018).
51. Fromm, D. P. et al. Gap-dependent optical coupling of single "bowtie" nanoantennas resonant in the visible. *Nano Lett.* **4**, 957–961 (2004).
52. Chen, X. S. et al. Atomic layer lithography of wafer-scale nanogap arrays for extreme confinement of electromagnetic waves. *Nat. Commun.* **4**, 2361 (2013).
53. Ward, D. R. et al. Optical rectification and field enhancement in a plasmonic nanogap. *Nat. Nanotechnol.* **5**, 732–736 (2010).
54. Lee, H. et al. All-optical control of high-purity trions in nanoscale waveguide. *Nat. Commun.* **14**, 1891 (2023).
55. Nam, J. M. et al. Plasmonic nanogap-enhanced Raman scattering with nanoparticles. *Acc. Chem. Res.* **49**, 2746–2755 (2016).
56. Lim, D. K. et al. Nanogap-engineerable Raman-active nanodumbbells for single-molecule detection. *Nat. Mater.* **9**, 60–67 (2010).
57. Regmi, R. et al. All-dielectric silicon nanogap antennas to enhance the fluorescence of single molecules. *Nano Lett.* **16**, 5143–5151 (2016).
58. Oh, Y. J. & Jeong, K. H. Glass nanopillar arrays with nanogap-rich silver nanoislands for highly intense surface enhanced Raman scattering. *Adv. Mater.* **24**, 2234–2237 (2012).
59. Li, Q. T. et al. A Purcell-enabled monolayer semiconductor free-space optical modulator. *Nat. Photonics* **17**, 897–903 (2023).
60. Akselrod, G. M. et al. Probing the mechanisms of large Purcell enhancement in plasmonic nanoantennas. *Nat. Photonics* **8**, 835–840 (2014).
61. Hoang, T. B. et al. Ultrafast spontaneous emission source using plasmonic nanoantennas. *Nat. Commun.* **6**, 7788 (2015).
62. Wang, Z. et al. Giant photoluminescence enhancement in tungsten-diselenide–gold plasmonic hybrid structures. *Nat. Commun.* **7**, 11283 (2016).
63. Kongsuwan, N. et al. Suppressed quenching and strong-coupling of Purcell-enhanced single-molecule emission in plasmonic nanocavities. *ACS Photonics* **5**, 186–191 (2018).
64. Vesseur, E. J. R., de Abajo, F. J. G. & Polman, A. Broadband Purcell enhancement in plasmonic ring cavities. *Phys. Rev. B* **82**, 165419 (2010).
65. Ji, B. T. et al. Non-blinking quantum dot with a plasmonic nanoshell resonator. *Nat. Nanotechnol.* **10**, 170–175 (2015).
66. Du, B. W. et al. Polarization-dependent Purcell enhancement on a two-dimensional h-BN/WS_2 light emitter with a dielectric plasmonic nanocavity. *Nano Lett.* **22**, 1649–1655 (2022).
67. Muskens, O. L. et al. Strong enhancement of the radiative decay rate of emitters by single plasmonic nanoantennas. *Nano Lett.* **7**, 2871–2875 (2007).
68. Russell, K. J. et al. Large spontaneous emission enhancement in plasmonic nanocavities. *Nat. Photonics* **6**, 459–462 (2012).
69. Dhawan, A. R. et al. Extreme multiexciton emission from deterministically assembled single-emitter subwavelength plasmonic patch antennas. *Light Sci. Appl.* **9**, 33 (2020).
70. Kim, W. G. et al. Three-dimensional plasmonic nanocluster-driven light–matter interaction for photoluminescence enhancement and picomolar-level biosensing. *Nano Lett.* **22**, 4702–4711 (2022).
71. Faggiani, R., Yang, J. J. & Lalanne, P. Quenching, plasmonic, and radiative decays in nanogap emitting devices. *ACS Photonics* **2**, 1739–1744 (2015).
72. Teperik, T. V., Popov, V. V. & de Abajo, F. J. G. Radiative decay of plasmons in a metallic nanoshell. *Phys. Rev. B* **69**, 155402 (2004).
73. Rose, A. et al. Control of radiative processes using tunable plasmonic nanopatch antennas. *Nano Lett.* **14**, 4797–4802 (2014).
74. Wang, J. Z. et al. Strong vibrational coupling in room temperature plasmonic resonators. *Nat. Commun.* **10**, 1527 (2019).
75. Mueller, N. S. et al. Deep strong light–matter coupling in plasmonic nanoparticle crystals. *Nature* **583**, 780–784 (2020).
76. Wen, B. Y. et al. Manipulating the light-matter interactions in plasmonic nanocavities at 1 nm spatial resolution. *Light Sci. Appl.* **11**, 235 (2022).
77. Xiang, B. et al. Intermolecular vibrational energy transfer enabled by microcavity strong light–matter coupling. *Science* **368**, 665–667 (2020).
78. Väkeväinen, A. I. et al. Plasmonic surface lattice resonances at the strong coupling regime. *Nano Lett.* **14**, 1721–1727 (2014).
79. Hou, S. Y. et al. Manipulating coherent light–matter interaction: continuous transition between strong coupling and weak coupling in MoS_2 monolayer coupled with plasmonic nanocavities. *Adv. Opt. Mater.* **7**, 1900857 (2019).
80. Salomon, A. et al. Strong light-molecule coupling on plasmonic arrays of different symmetry. *ChemPhysChem* **14**, 1882–1886 (2013).
81. Park, K. D. et al. Hybrid tip-enhanced nanospectroscopy and nanoimaging of monolayer WSe_2 with local strain control. *Nano Lett.* **16**, 2621–2627 (2016).
82. Park, W. H. & Kim, Z. H. Charge transfer enhancement in the SERS of a single molecule. *Nano Lett.* **10**, 4040–4048 (2010).
83. Zhu, W. Q. et al. Quantum mechanical effects in plasmonic structures with subnanometre gaps. *Nat. Commun.* **7**, 11495 (2016).
84. Kravtsov, V. et al. Control of plasmon emission and dynamics at the transition from classical to quantum coupling. *Nano Lett.* **14**, 5270–5275 (2014).
85. Mortensen, N. A. et al. A generalized non-local optical response theory for plasmonic nanostructures. *Nat. Commun.* **5**, 3809 (2014).
86. May, M. A. et al. Nanocavity clock spectroscopy: resolving competing exciton dynamics in WSe_2/$MoSe_2$ heterobilayers. *Nano Lett.* **21**, 522–528 (2021).
87. Zhang, M. et al. Observation of ultra-large Rabi splitting in the plasmon-exciton polaritons at room temperature. *Nanophotonics* **12**, 3267–3275 (2023).
88. Berghuis, A. M. et al. Light–matter coupling strength controlled by the orientation of organic crystals in plasmonic cavities. *J. Phys. Chem. C* **124**, 12030–12038 (2020).
89. Cui, G. Q. & Raymer, M. G. Emission spectra and quantum efficiency of single-photon sources in the cavity-QED strong-coupling regime. *Phys. Rev. A* **73**, 053807 (2006).
90. He, Z. et al. Quantum plasmonic control of trions in a picocavity with monolayer WS_2. *Sci. Adv.* **5**, eaau8763 (2019).
91. Huang, S. et al. Identifying single bases in a DNA oligomer with electron tunnelling. *Nat. Nanotechnol.* **5**, 868–873 (2010).
92. Zhang, B. T. et al. Electronic conductance resonance in non-redox-active proteins. *J. Am. Chem. Soc.* **142**, 6432–6438 (2020).
93. Kang, M. et al. Conformational heterogeneity of molecules physisorbed on a gold surface at room temperature. *Nat. Commun.* **13**, 4133 (2022).
94. Tang, L. H. et al. Combined quantum tunnelling and dielectrophoretic trapping for molecular analysis at ultra-low analyte concentrations. *Nat. Commun.* **12**, 913 (2021).
95. Tang, L. H. et al. Measuring conductance switching in single proteins using quantum tunneling. *Sci. Adv.* **8**, eabm8149 (2022).
96. Hutchison, J. A. et al. Modifying chemical landscapes by coupling to vacuum fields. *Angew. Chem. Int. Ed.* **51**, 1592–1596 (2012).
97. Hennessy, K. et al. Quantum nature of a strongly coupled single quantum dot–cavity system. *Nature* **445**, 896–899 (2007).
98. Peng, Z. W. et al. Strain engineering of 2D semiconductors and graphene: from strain fields to band-structure tuning and photonic applications. *Light Sci. Appl.* **9**, 190 (2020).
99. Shen, T. T., Penumatcha, A. V. & Appenzeller, J. Strain engineering for transition metal dichalcogenides based field effect transistors. *ACS Nano* **10**, 4712–4718 (2016).
100. Qi, J. J. et al. Piezoelectric effect in chemical vapour deposition-grown atomic-monolayer triangular molybdenum disulfide piezotronics. *Nat. Commun.* **6**, 7430 (2015).
101. Steele, J. A. et al. Thermal unequilibrium of strained black $CsPbI_3$ thin films. *Science* **365**, 679–684 (2019).
102. Xiao, Z. G. et al. Solvent annealing of perovskite-induced crystal growth for photovoltaic-device efficiency enhancement. *Adv. Mater.* **26**, 6503–6509 (2014).
103. Cao, Y. et al. Pressure-induced emission enhancements of Mn^{2+}-doped cesium lead chloride perovskite nanocrystals. *ACS Mater. Lett.* **2**, 381–388 (2020).
104. Liu, G. et al. Isothermal pressure-derived metastable states in 2D hybrid perovskites showing enduring bandgap narrowing. *Proc. Natl Acad. Sci. USA* **115**, 8076–8081 (2018).
105. Zhang, Z. X. et al. Uniaxial strain and hydrostatic pressure engineering of the hidden magnetism in $La_{1-x}Ca_xMnO_3$ ($0 \le x \le 1/2$) thin films. *Nano Lett.* **22**, 7328–7335 (2022).
106. Yan, H. et al. Sterically controlled mechanochemistry under hydrostatic pressure. *Nature* **554**, 505–510 (2018).

107. Lee, J. et al. Switchable, tunable, and directable exciton funneling in periodically wrinkled WS_2. *Nano Lett.* **21**, 43–50 (2021).
108. Chen, Y. M. et al. Strain engineering and epitaxial stabilization of halide perovskites. *Nature* **577**, 209–215 (2020).
109. Desai, S. B. et al. Strain-induced indirect to direct bandgap transition in multilayer WSe_2. *Nano Lett.* **14**, 4592–4597 (2014).
110. Li, Z. W. et al. Efficient strain modulation of 2D materials via polymer encapsulation. *Nat. Commun.* **11**, 1151 (2020).
111. Yang, S. X. et al. Tuning the optical, magnetic, and electrical properties of $ReSe_2$ by nanoscale strain engineering. *Nano Lett.* **15**, 1660–1666 (2015).
112. Song, S. et al. Room temperature semiconductor–metal transition of $MoTe_2$ thin films engineered by strain. *Nano Lett.* **16**, 188–193 (2016).
113. Chen, B. et al. Large electrostrictive response in lead halide perovskites. *Nat. Mater.* **17**, 1020–1026 (2018).
114. Lee, C. et al. Measurement of the elastic properties and intrinsic strength of monolayer graphene. *Science* **321**, 385–388 (2008).
115. Zhang, Y. Q. et al. Intriguing heterophase domain patterns in correlated electron material via tip force engineering. *Acta Mater.* **235**, 118089 (2022).
116. Roy, R., Nečas, D. & Zajíčková, L. Evidence of flexoelectricity in graphene nanobubbles created by tip induced electric field. *Carbon* **179**, 677–682 (2021).
117. Manzeli, S. et al. Piezoresistivity and strain-induced band gap tuning in atomically thin MoS_2. *Nano Lett.* **15**, 5330–5335 (2015).
118. Ko, W. et al. Tip-induced local strain on MoS_2/graphite detected by inelastic electron tunneling spectroscopy. *Phys. Rev. B* **97**, 125401 (2018).
119. Alyabyeva, N. et al. Metal-insulator transition in V_2O_3 thin film caused by tip-induced strain. *Appl. Phys. Lett.* **113**, 241603 (2018).
120. Zhou, Y. Q. et al. Tip-induced in-plane ferroelectric superstructure in zigzag-wrinkled $BaTiO_3$ thin films. *Nano Lett.* **22**, 2859–2866 (2022).
121. Klimov, N. N. et al. Electromechanical properties of graphene drumheads. *Science* **336**, 1557–1561 (2012).
122. Lu, H. et al. Mechanical writing of ferroelectric polarization. *Science* **336**, 59–61 (2012).
123. Wang, Y. L. et al. Strain-induced direct–indirect bandgap transition and phonon modulation in monolayer WS_2. *Nano Res.* **8**, 2562–2572 (2015).
124. Sun, Z. et al. Stress-induced bandgap renormalization in atomic crystals. *Solid State Commun.* **288**, 18–21 (2019).
125. Lee, H. et al. Tip-induced strain engineering of a single metal halide perovskite quantum dot. *ACS Nano* **15**, 9057–9064 (2021).
126. Nickel, R. et al. Nanoscale size effects on push–pull Fe–O hybridization through the multiferroic transition of perovskite ϵ-Fe_2O_3. *Nano Lett.* **23**, 7845–7851 (2023).
127. Bauer, S. & Bobisch, C. A. Nanoscale electron transport at the surface of a topological insulator. *Nat. Commun.* **7**, 11381 (2016).
128. Yuan, R. H. et al. Nanoscale phase separation of antiferromagnetic order and superconductivity in $K_{0.75}Fe_{1.75}Se_2$. *Sci. Rep.* **2**, 221 (2012).
129. Koo, Y. et al. Tunable interlayer excitons and switchable interlayer trions via dynamic near-field cavity. *Light Sci. Appl.* **12**, 59 (2023).
130. Young, A. B. et al. Polarization engineering in photonic crystal waveguides for spin-photon entanglers. *Phys. Rev. Lett.* **115**, 153901 (2015).
131. Strauf, S. et al. High-frequency single-photon source with polarization control. *Nat. Photonics* **1**, 704–708 (2007).
132. Shitrit, N. et al. Spin-optical metamaterial route to spin-controlled photonics. *Science* **340**, 724–726 (2013).
133. Lin, J. et al. Polarization-controlled tunable directional coupling of surface plasmon polaritons. *Science* **340**, 331–334 (2013).
134. Sukharev, M. & Seideman, T. Phase and polarization control as a route to plasmonic nanodevices. *Nano Lett.* **6**, 715–719 (2006).
135. Karimi, E. et al. Generating optical orbital angular momentum at visible wavelengths using a plasmonic metasurface. *Light Sci. Appl.* **3**, e167 (2014).
136. Chen, Y. J. et al. Valley-polarized exciton–polaritons in a monolayer semiconductor. *Nat. Photonics* **11**, 431–435 (2017).
137. Liu, C. et al. Polarization-resolved broadband MoS_2/black phosphorus/MoS_2 optoelectronic memory with ultralong retention time and ultrahigh switching ratio. *Adv. Funct. Mater.* **31**, 2100781 (2021).
138. Yao, W., Xiao, D. & Niu, Q. Valley-dependent optoelectronics from inversion symmetry breaking. *Phys. Rev. B* **77**, 235406 (2008).
139. Wu, J. X. et al. Identifying the crystalline orientation of black phosphorus using angle-resolved polarized Raman spectroscopy. *Angew. Chem. Int. Ed.* **54**, 2366–2369 (2015).
140. Guan, M. L. et al. Polarization modulation with optical lock-in detection reveals universal fluorescence anisotropy of subcellular structures in live cells. *Light Sci. Appl.* **11**, 4 (2022).
141. Kim, J. et al. Anomalous polarization dependence of Raman scattering and crystallographic orientation of black phosphorus. *Nanoscale* **7**, 18708–18715 (2015).
142. Robert, C. et al. Spin/valley pumping of resident electrons in WSe_2 and WS_2 monolayers. *Nat. Commun.* **12**, 5455 (2021).
143. Dąbrowski, M. et al. All-optical control of spin in a 2D van der Waals magnet. *Nat. Commun.* **13**, 5976 (2022).
144. Islam, R. et al. Tunable spin polarization and electronic structure of bottom-up synthesized $MoSi_2N_4$ materials. *Phys. Rev. B* **104**, L201112 (2021).
145. Li, L. et al. Highly in-plane anisotropic 2D $GeAs_2$ for polarization-sensitive photodetection. *Adv. Mater.* **30**, 1804541 (2018).
146. Rivera, P. et al. Valley-polarized exciton dynamics in a 2D semiconductor heterostructure. *Science* **351**, 688–691 (2016).
147. Liu, X. Y. et al. WS_2/hBN hetero-nanoslits with spatially mismatched electromagnetic multipoles for directional and enhanced light emission. *ACS Nano* **16**, 675–682 (2022).
148. Li, Y. B. et al. Dimensional reduction of $Cs_2AgBiBr_6$: a 2D hybrid double perovskite with strong polarization sensitivity. *Angew. Chem. Int. Ed.* **59**, 3429–3433 (2020).
149. Zakharko, Y., Graf, A. & Zaumseil, J. Plasmonic crystals for strong light–matter coupling in carbon nanotubes. *Nano Lett.* **16**, 6504–6510 (2016).
150. Schietinger, S. et al. Plasmon-enhanced single photon emission from a nanoassembled metal–diamond hybrid structure at room temperature. *Nano Lett.* **9**, 1694–1698 (2009).
151. Liu, X. J. et al. Near-field modulation of differently oriented single photon emitters with a plasmonic probe. *Nano Lett.* **22**, 2244–2250 (2022).
152. Ge, D. D. et al. Hybrid plasmonic nano-emitters with controlled single quantum emitter positioning on the local excitation field. *Nat. Commun.* **11**, 3414 (2020).
153. Liu, E. F. et al. Excitonic and valley-polarization signatures of fractional correlated electronic phases in a WSe_2/WS_2 moiré superlattice. *Phys. Rev. Lett.* **127**, 037402 (2021).
154. Miao, S. N. et al. Strong interaction between interlayer excitons and correlated electrons in WSe_2/WS_2 moiré superlattice. *Nat. Commun.* **12**, 3608 (2021).
155. Yu, H. Y. & Yao, W. Luminescence anomaly of dipolar valley excitons in homobilayer semiconductor moiré superlattices. *Phys. Rev. X* **11**, 021042 (2021).
156. Torun, E. et al. Interlayer and intralayer excitons in MoS_2/WS_2 and $MoSe_2$/WSe_2 heterobilayers. *Phys. Rev. B* **97**, 245427 (2018).
157. Park, K. D. & Raschke, M. B. Polarization control with plasmonic antenna tips: a universal approach to optical nanocrystallography and vector-field imaging. *Nano Lett.* **18**, 2912–2917 (2018).
158. Sanders, A. et al. Understanding the plasmonics of nanostructured atomic force microscopy tips. *Appl. Phys. Lett.* **109**, 153110 (2016).
159. Fiebig, M. et al. Probing of ferroelectric surface and bulk domains in $RMnO_3$ (R=Y, Ho) by second harmonic generation. *Phys. Rev. B* **66**, 144102 (2002).
160. Neacsu, C. C. et al. Second-harmonic near-field imaging of ferroelectric domain structure of $YMnO_3$. *Phys. Rev. B* **79**, 100107 (2009).
161. Krasnok, A. E. et al. Optical nanoantennas. *Phys. Usp.* **56**, 539–564 (2013).
162. Singh, A., Calbris, G. & van Hulst, N. F. Vectorial nanoscale mapping of optical antenna fields by single molecule dipoles. *Nano Lett.* **14**, 4715–4723 (2014).
163. Sick, B., Hecht, B. & Novotny, L. Orientational imaging of single molecules by annular illumination. *Phys. Rev. Lett.* **85**, 4482–4485 (2000).
164. Novotny, L. et al. Longitudinal field modes probed by single molecules. *Phys. Rev. Lett.* **86**, 5251–5254 (2001).
165. Lee, H. et al. Inducing and probing localized excitons in atomically thin semiconductors via tip-enhanced cavity-spectroscopy. *Adv. Funct. Mater.* **31**, 2102893 (2021).
166. Kern, J. et al. Nanoscale positioning of single-photon emitters in atomically thin WSe_2. *Adv. Mater.* **28**, 7101–7105 (2016).
167. Lee, D. Y. et al. Adaptive tip-enhanced nano-spectroscopy. *Nat. Commun.* **12**, 3465 (2021).
168. Koo, Y. et al. Nanocavity-integrated van der Waals heterobilayers for nano-excitonic transistor. *ACS Nano* **17**, 4854–4861 (2023).
169. Vellekoop, I. M. & Mosk, A. P. Phase control algorithms for focusing light through turbid media. *Opt. Commun.* **281**, 3071–3080 (2008).

170. Gjonaj, B. et al. Active spatial control of plasmonic fields. *Nat. Photonics* **5**, 360–363 (2011).
171. Man, Z. S. et al. Dynamic plasmonic beam shaping by vector beams with arbitrary locally linear polarization states. *Appl. Phys. Lett.* **105**, 011110 (2014).
172. Sahin, H. et al. Anomalous Raman spectra and thickness-dependent electronic properties of WSe_2. *Phys. Rev. B* **87**, 165409 (2013).
173. Del Corro, E. et al. Excited excitonic states in 1L, 2L, 3L, and bulk WSe2 observed by resonant Raman spectroscopy. *ACS Nano* **8**, 9629–9635 (2014).
174. Mogi, H. et al. Ultrafast nanoscale exciton dynamics via laser-combined scanning tunneling microscopy in atomically thin materials. *npj 2D Mater. Appl.* **6**, 72 (2022).
175. Román, R. J. P. et al. Tip-induced and electrical control of the photoluminescence yield of monolayer WS_2. *Nano Lett.* **22**, 9244–9251 (2022).
176. Kravtsov, V. et al. Plasmonic nanofocused four-wave mixing for femtosecond near-field imaging. *Nat. Nanotechnol.* **11**, 459–464 (2016).
177. Luo, W. J. et al. Ultrafast nanoimaging of electronic coherence of monolayer WSe_2. *Nano Lett.* **23**, 1767–1773 (2023).
178. Shaltout, A. M. et al. Spatiotemporal light control with active metasurfaces. *Science* **364**, eaat3100 (2019).
179. Park, J. et al. All-solid-state spatial light modulator with independent phase and amplitude control for three-dimensional LiDAR applications. *Nat. Nanotechnol.* **16**, 69–76 (2021).
180. Binnig, G., Quate, C. F. & Gerber, C. Atomic force microscope. *Phys. Rev. Lett.* **56**, 930–933 (1986).
181. Tersoff, J. & Hamann, D. R. Theory and application for the scanning tunneling microscope. *Phys. Rev. Lett.* **50**, 1998–2001 (1983).
182. Zhou, Y. et al. Probing dark excitons in atomically thin semiconductors via near-field coupling to surface plasmon polaritons. *Nat. Nanotechnol.* **12**, 856–860 (2017).
183. Madéo, J. et al. Directly visualizing the momentum-forbidden dark excitons and their dynamics in atomically thin semiconductors. *Science* **370**, 1199–1204 (2020).
184. Reithmaier, J. P. et al. Strong coupling in a single quantum dot–semiconductor microcavity system. *Nature* **432**, 197–200 (2004).
185. Peter, E. et al. Exciton-photon strong-coupling regime for a single quantum dot embedded in a microcavity. *Phys. Rev. Lett.* **95**, 067401 (2005).
186. Li, Q. S. et al. AFM indentation study of breast cancer cells. *Biochem. Biophys. Res. Commun.* **374**, 609–613 (2008).
187. Falin, A. et al. Mechanical properties of atomically thin tungsten dichalcogenides: WS_2, WSe_2, and WTe_2. *ACS Nano* **15**, 2600–2610 (2021).
188. Reitzenstein, S. et al. Control of the strong light-matter interaction between an elongated $In_{0.3}Ga_{0.7}As$ quantum dot and a micropillar cavity using external magnetic fields. *Phys. Rev. Lett.* **103**, 127401 (2009).
189. Rajabali, S. et al. Polaritonic nonlocality in light–matter interaction. *Nat. Photonics* **15**, 690–695 (2021).
190. Kolosov, O. et al. Nanoscale visualization and control of ferroelectric domains by atomic force microscopy. *Phys. Rev. Lett.* **74**, 4309–4312 (1995).
191. Kim, J. H. et al. Nontrivial, unconventional electrochromic behaviors of plasmonic nanocubes. *Nano Lett.* **21**, 7512–7518 (2021).
192. Taguchi, A. et al. Deep-UV tip-enhanced Raman scattering. *J. Raman Spectrosc.* **40**, 1324–1330 (2009).
193. Elias, C. et al. Flat bands and giant light-matter interaction in hexagonal boron nitride. *Phys. Rev. Lett.* **127**, 137401 (2021).
194. Ma, W. L. et al. In-plane anisotropic and ultra-low-loss polaritons in a natural van der Waals crystal. *Nature* **562**, 557–562 (2018).
195. Huth, F. et al. Resonant antenna probes for tip-enhanced infrared near-field microscopy. *Nano Lett.* **13**, 1065–1072 (2013).
196. Ladani, F. T. & Potma, E. O. Dyadic Green's function formalism for photoinduced forces in tip-sample nanojunctions. *Phys. Rev. B* **95**, 205440 (2017).
197. Zhang, J. W. et al. Terahertz nanoimaging of graphene. *ACS Photonics* **5**, 2645–2651 (2018).
198. Jahng, J. et al. Direct chemical imaging of ligand-functionalized single nanoparticles by photoinduced force microscopy. *J. Phys. Chem. Lett.* **11**, 5785–5791 (2020).
199. Romero, E. et al. Quantum coherence in photosynthesis for efficient solar-energy conversion. *Nat. Phys.* **10**, 676–682 (2014).
200. Romero, E., Novoderezhkin, V. I. & van Grondelle, R. Quantum design of photosynthesis for bio-inspired solar-energy conversion. *Nature* **543**, 355–365 (2017).